Changes in stratiform heating structure due to surface warming weaken and accelerate convectively coupled Kelvin waves

Mu-Ting Chien[1] and Daehyun Kim[2,3]

1Department of Atmospheric Science, Colorado State University

2Department of Atmospheric and Climate Sciences, University of Washington

3School of Earth and Environmental Sciences, Seoul National University, South Korea

E-mail: muting.climate.science@gmail.com

Submitted to a peer-reviewed journal *npj Climate and Atmospheric Science on June 20, 2025*

Changes in stratiform heating structure due to surface warming weaken and accelerate convectively coupled Kelvin waves

Mu-Ting Chien[a] and Daehyun Kim[b,c] *

[a]Department of Atmospheric Science, Colorado State University

[b]School of Earth and Environmental Sciences, Seoul National University, South Korea

[c]Department of Atmospheric and Climate Science, University of Washington

*Corresponding author: Daehyun Kim (daehyun@snu.ac.kr)

Abstract

Although stratiform heating plays a crucial role in tropical convective systems, we do not fully understand (1) how stratiform heating would change in response to surface warming and (2) how those changes would affect convectively-coupled equatorial waves. This study analyzes the changes in stratiform heating structure and convectively-coupled Kelvin waves (KWs) associated with surface warming using a set of aquaplanet simulations. Results show that the melting level rises with warming, causing ice particles falling from the stratiform clouds to melt at lower pressure levels. The upward shift of melting-induced cooling results in a decrease in temperature and vertical motion variability associated with stratiform clouds in the lower free-troposphere and upper boundary layer. These changes lower the degree to which stratiform (i.e., the second baroclinic mode) and deep convective clouds (i.e., the first baroclinic mode) are coupled within KWs, causing KWs to weaken and accelerate with warming.

Introduction

Deep convective clouds and trailing stratiform clouds are building blocks of the tropical precipitating systems, ranging from mesoscale convective systems[1], which last a few hours, to the synoptic-scale convectively coupled equatorial waves (CCEWs)[1,2], which last several days to weeks, and planetary-scale Madden-Julian Oscillation (MJO)[3,4], which lasts 30-90 days. Deep convective clouds and stratiform clouds present distinct diabatic heating characteristics[5,6]. Their respective heating structures can be empirically obtained as those that explain most variance in diabatic heating anomalies[7-9]: the first and second baroclinic modes or analytically obtained from the mean state temperature profile[10-12]. The first baroclinic mode is characterized by single-signed heating/cooling anomalies across the whole troposphere; the second baroclinic mode is characterized by a dipole of heating and cooling anomalies across the troposphere, separated by the melting level. The second baroclinic heating aloft is contributed by water vapor deposition upon ice particles falling from the convective region, and the second baroclinic cooling below is contributed by melting and evaporation of stratiform rain.[13,14]

Characterizing the two modes' vertical structures of diabatic heating is crucial for the climate system from the annual to subseasonal timescales. On the annual timescale, the fraction of stratiform rain could affect the vertical structure of the total latent heat, thus impacting the response of the mean circulation[5]. On the subseasonal timescales, the basic structures of CCEWs and MJO in observations and numerical simulations can be approximately reconstructed with the two baroclinic modes[8,11,15,16]. Due to this reason, previous studies construct linear simple models based on the two modes to explain the maintenance and propagation mechanisms of the convectively coupled Kelvin waves (KWs)[17-22] — the eastward-propagating envelopes of enhanced and suppressed convection maximized at the equator with an in-phase relationship between geopotential and zonal wind anomalies.

Because deep convection is the most dominant mode in the tropics, earlier theories argued that KWs grow by positive thermodynamic feedback between diabatic heating and temperature anomalies of the first baroclinic mode component[17-19]. In their theories, the second baroclinic mode passively responds to the first mode, and it does not contribute to KW dynamics. However, recent studies suggest that this positive thermodynamic feedback occurs within the second baroclinic mode component of the KWs and that the interactions between the first and second baroclinic modes are essential[9,20-23]). The proposed instability mechanism – the interactions between the two baroclinic modes – can be briefly summarized as follows: deep convective clouds produce ice condensates that are detrained into the environment. The detrained ice condensates form stratiform clouds which produce diabatic heating and cooling above and below the melting level, respectively. The second baroclinic mode heating anomalies change the environmental temperature, affecting the stability, and thereby the triggering of deep convection. However, detailed physical processes on how the second baroclinic heating affects temperature and thus affects deep convection differ between different simple models, especially how moisture is at play. For example, moisture does not affect convection at all in a simple model[22]; mid-level moisture deficit regulates the height of convection in another model[21]; another model considered column moisture vital for convection[20]. These diverse representations in simple models highlight that we do not fully understand how the two modes interact with each other within KWs.

Given the importance of characterizing the two modes' vertical structures of diabatic heating from annual to subseasonal timescales, it is vital to understand how their structures would change under greenhouse-gas-induced warming. However, the projection of the heating structure changes with warming is uncertain because we do not fully understand the interaction between the mean state temperature changes and the changes in convective systems. Under greenhouse-gas-induced warming, studies have attempted to explain the change of the mean state temperature vertical profile. For example, studies have shown that the tropopause and the melting level would rise and that the static stability in the troposphere would increase in response to warming due to more substantial warming in the upper troposphere than in the lower troposphere[24-26]. A large portion of the mean state temperature change in the tropics can be explained by the vertical shift in temperature and humidity[27,28]. On the other hand, the way in which the mean state changes affect the vertical structure of convective systems is less understood. A recent study found that the rise of the melting level could enhance extreme precipitation as it increases the depth in which rain droplets can grow before reaching the surface[29]. However, the changes in diabatic heating of the two modes in response to warming are not explicitly discussed. Characterizing and understanding the changes to the two modes' vertical structures of diabatic heating with warming is equivalent to understanding the interaction between the mean state changes and the changes in convective systems.

Furthermore, projected changes in KWs under global warming are ongoing open questions. One study[30] found that KWs intensify and accelerate in global climate models of the sixth version of the coupled model intercomparison project (CMIP6[31]). However, the mechanisms behind the changes are unclear, underscoring a lack of understanding of the response of KWs to the mean state changes. Most recently, using a set of aquaplanet simulations with prescribed sea surface temperatures, another study found that KWs weaken and accelerate with surface warming[32]. Their results suggest that the weakening and acceleration of KWs to surface warming are related to the weaker coupling between the two baroclinic modes, which makes KWs follow the second baroclinic mode dynamics in a cooler climate and the first baroclinic mode dynamics in a warmer climate[32]. In other words, KWs in a colder climate grow by positive thermodynamic feedback within the second baroclinic mode, while KWs in a warmer climate are damped by negative thermodynamic feedback within the first baroclinic mode[32]. Meanwhile, KWs in a colder climate propagate more slowly as they follow the second baroclinic mode phase speed, while KWs in a warmer climate propagate faster as they follow the first baroclinic mode phase speed[32]. While their study associated the response of KWs to surface warming with the weaker coupling between the two baroclinic modes[32], it remains unclear what physical processes control the coupling and why the coupling weakens with warming.

Despite the potential impact of stratiform heating on the mean climate and KW dynamics, the changes in stratiform heating as the climate warms and their influence remain unexplored in the literature. This study uses aquaplanet simulations with surface warming and cooling experiments (+4K, -4K, CTL) to investigate (1) the changes in the stratiform heating structure with warming and (2) how these changes affect KWs. Specifically, we investigate how changes in stratiform heating affect the coupling between the first and second baroclinic modes within KWs. Based on the coevolution of moisture, precipitation, temperature, and convective heating within KWs, we propose a mechanism for how the two baroclinic modes couple within KWs and explain why coupling weakens with warming. Ultimately, we explain the amplitude and phase speed changes of KWs as the surface warms based on the changes in coupling due to the mean state change.

Results

The first and second baroclinic mode structures change with warming

To obtain the dominant vertical structures of diabatic heating anomalies that explain the largest variance in the tropics, the empirical orthogonal function (EOF) analysis is conducted on diabatic heating anomalies. The most dominant vertical structure of diabatic heating anomalies in our simulation is the first baroclinic mode, which shows a single-signed structure across the whole troposphere (Fig. 1a). The second most dominant mode is the second baroclinic mode, with a dipole in the upper and lower troposphere, separated by a nodal point in the mid-troposphere (Fig. 1b). The vertical structures of the two modes are roughly consistent with those in observations or reanalyses[5,9,13-14]. Because the two baroclinic modes are obtained empirically based on EOF analysis, from now on, we will use the EOF1 (EOF2) and the first (second) baroclinic mode interchangeably.

Figure 1a shows that the two EOFs in all experiments are roughly bounded at the surface and the tropopause (around 100hPa), suggesting that the top and bottom of deep convection remain similar. However, the peak of the EOF1 shifts upward from around 600 hPa in -4K to around 450 hPa in +4K (Fig. 1a), suggesting that the structure of deep convection changes from more bottom-heavy to more top-heavy. Figure 1b shows that from -4K to +4K, with the surface and tropopause remaining similar, the vertical structure of EOF2 also changes with warming: the peak of positive and negative anomalies and the nodal point move upward. As a result, the positive anomalies aloft shrink while the negative anomalies below expand. That is, the lower-level peak of EOF2 is in the midpoint between the surface and the nodal point in -4K (blue line in Fig. 1b). In comparison, the lower-level peak is located much closer to the nodal point in +4K (red line in Fig. 1b). The weaker magnitude of the EOF2 in the lower troposphere around 800 hPa (marked with the orange square in Fig. 1) suggests that the second baroclinic mode diabatic heating anomalies would have a weaker impact on the temperature variability in the lower troposphere as the surface warms.

The second baroclinic mode structure changes as the melting level rises with warming

To understand the physical processes that lead to the structural changes in EOF1 and EOF2 with warming, we decompose the total diabatic heating anomalies into temperature tendencies from individual physical parameterization schemes. The temperature tendency (heating) from moist physics includes temperature tendency from (1) deep convection from Zhang and McFarlane (1995) scheme[33] (abbreviated as ZM scheme from now on), (2) evaporation of convective rain in ZM scheme, (3) shallow convection, boundary layer, and cloud macrophysics from the Cloud Layers Unified by Binormals (CLUBB) scheme[34,35], and (4) the advanced two-moment prognostic cloud microphysics from Gettleman and Morrison 2015[36] (MG2).

Figure 2 shows the anomalies of each temperature tendency term regressed upon precipitation anomalies on different lag days for the entire tropics. In -4K, before lag day 0 (at maximum precipitation), there is enhanced diabatic heating around 800 hPa, and at lag day 0, enhanced diabatic heating occurs throughout the troposphere (Fig. 2a-c). Figure 2d-f shows that the heating from the ZM deep convection scheme has the highest magnitude among all other tendency terms (Fig. 2g-o). At lag day 0, the ZM scheme produces single-signed heating across the entire troposphere, which likely contributes to the first baroclinic mode structure. The maximum ZM heating occurs around 600 hPa (Fig. 2d-f). The weakening of ZM heating in the lower troposphere below the melting level, especially in -4K (Fig. 2d), is due to the evaporation of convective rain from the ZM scheme, as shown in the cooling anomalies below the melting level in the temperature tendency from evaporation of convective rain in the ZM scheme in Fig. 2g. Figure 2j-l shows that temperature tendency from CLUBB presents an overall heating at lag day 0, with a maximum around 500 hPa, above the maximum heating from the ZM scheme. CLUBB produces heating from shallow convection, cloud macrophysics (the previous "stratiform" parameterization scheme in CAM5), and boundary layer processes. The maximum heating around 500 hPa is likely from the condensation of stratiform cloud processes. Shading in Figure 2m-o shows the temperature tendency from the cloud microphysics scheme, which shows a weak heating in the upper troposphere and a weak cooling in the lower troposphere, with the most robust cooling located around 800 hPa. The contours in Fig. 2m-o represent the latent heat from melting, showing the strongest cooling around 800 hPa, and perfectly match the cooling anomalies from cloud microphysics.

The maximum diabatic heating is at lower pressure levels compared in +4K (Fig. 2c) to that in -4K (Fig. 2a). Meanwhile, in +4K, the total heating is more tilted, with substantial heating in the lower troposphere before maximum precipitation and substantial heating in the upper troposphere after maximum precipitation. Heating from the ZM scheme is strongest at around 450 hPa in +4K (Fig. 2f), shifted upward from 600 hPa in -4K (Fig. 2d). Associated with the upward shift of the maximum heating of deep convection due to surface warming, the most substantial cooling from evaporation of convective rain (Fig. 2i), stratiform heating (Fig. 2l), and melting (Fig. 2o, contour) are all located at lower pressure levels in +4K compared to those in -4K (Fig. 2g, j, m).

To understand the contribution of each temperature tendency term to EOF1 and EOF2, we project the lag-regressed temperature tendency terms in Fig. 2 onto EOF1 and EOF2 (Fig. S1 and S2). Figure S1 shows that the tendency from the ZM deep convection (blue line) contributes the most to the variability of EOF1, while CLUBB (yellow line) contributes secondarily. Cloud microphysics and rain evaporation of the convective rain from the ZM scheme contribute minimally to the variability of EOF1. This confirms that EOF1 mostly comes from the ZM scheme, which represents deep convection. On the other hand, EOF2 is mainly contributed by the tendency from the cloud microphysics scheme (red line) and CLUBB (yellow line), which is likely from stratiform cloud processes (Fig. S2).

After identifying the dominant physical processes contributing to EOF1 and EOF2, Figure 3 shows the similarity in the vertical structure of those dominant physical processes and EOF2. The corresponding result for EOF1 is shown in Fig. S3. The overall single-signed heating structure of EOF1 (Fig. S3c) resembles the structure from the ZM deep convection scheme (Fig. S3b, obtained from Fig. 2 at lag day 0). Furthermore, the maximum EOF1 (Fig. S3c) is roughly located at the same pressure level as the maximum heating from the ZM scheme (Fig. S3b), confirming again that the EOF1 mostly comes from the ZM scheme. On the other hand, the overall positive-aloft-negative-below structure of EOF2 (Fig. 3c) is similar to the vertical structure of the regressed heating from the cloud microphysics scheme (Fig. 3b), which shows that the lower tropospheric cooling is located below the melting level (indicated in crosses, identified from the 0^{o}C of the mean state temperature averaged over 10˚S-10˚N). Note that melting starts right at the melting level in CTL and +4K and occurs some layers below the melting level in -4K where the mean temperature is roughly 2 deg C (Fig. 2b). This is likely because that there is more snow in -4K and that snow starts melting at 2°C in CAM6 while there is more cloud ice in CTL and +4K, which starts melting at 0°C (this is a default setting of CAM6 in their model code). Nevertheless, the minimum of EOF2 (i.e., the negative peak in Fig. 3c in the lower troposphere) is located at a similar pressure level with the negative peak in cloud microphysics scheme (Fig. 3b), which comes explicitly from cooling due to melting (confirmed by contours overlapping with shading in Fig. 2e). The maximum of EOF2 (i.e., the positive peak in Fig. 3c in the upper troposphere) corresponds to the peak of the regressed heating from CLUBB (Fig. 3a, obtained from Fig. 2 at lag day 0), likely from stratiform processes, as evidenced that the most substantial heating from CLUBB is located above the melting level. The upper tropospheric peak of EOF2 aligns with maximum heating from CLUBB; the lower tropospheric peak of EOF2 aligns with the maximum cooling due to melting (Fig. 3b). As the surface warms, the melting level rises from 650 hPa in -4K to 575 hPa in CTL, and 525 hPa in +4K (roughly -2.7%hPa/K) (Fig. 3d). As the melting level rises, the peaks of the second EOF also rise to the upper troposphere (Fig. 3c). Particularly that the change in EOF2 with warming in the lower troposphere is primarily due to melting, which primarily depends on the mean state temperature profile. In addition, the location of the EOF2 peak in the lower troposphere (i.e., how far below the melting level does maximum melting occur) may also depend on the amount of ice to be melted, which is associated with how strong the deep convection is.

Regardless, the mean state temperature change sets the changes in the EOF2 structure to the first order. Figure S4 shows the simulated mean state temperature change from CTL to +4K and from CTL to -4K (red and blue lines, respectively). While the surface warms by 4K, warming in the upper troposphere (>100 hPa) is larger than 4K. The temperature change can be approximately explained by the pure vertical shift of temperature with the additional effect due to the shift of moisture, which induces latent heat, described as vertical structure transform (VST)[27,28]. This is because that specific humidity and relative humidity also roughly shift upward. Around the melting level (500 to 700 hPa), there is a thick layer of roughly constant warming, and the theoretical temperature change from VST aligns particularly well with the simulated temperature change. Additional information on the VST in our simulations is described in Text S4. This suggests that the melting level rise in our simulations can be explained by the pure vertical shift of temperature with the additional effect due to the vertical shift of moisture. Figure S5 shows the EOF2 structure as a function of the mean state temperature, in which the lower tropospheric peak of the EOF2 in each simulation converges at around the same temperature. These support the argument that as the surface warms, the change of the EOF2 structure is due to the change in the mean state temperature.

Coupling between the two modes weakens with warming within KWs

The interaction between the first and second baroclinic modes is a fundamental aspect of KW dynamics in several simple models[20-22]. The interaction between the two modes can be summarized in Fig. S6: (a) the second baroclinic mode temperature perturbation triggers deep convection (also known as the first baroclinic mode heating), (b) deep convection affects the stratiform heating (also known as the second baroclinic mode heating), and (c) the second baroclinic mode heating amplifies the second baroclinic mode temperature. Note that precipitation is mainly driven by deep convection; thus, maximum precipitation occurs when deep convection is strongest. In the later paragraphs, precipitation and deep convection are used interchangeably.

Investigating how the interaction (coupling) between the two modes changes with warming is key to understanding the changes in KWs. We quantify the coupling strength by the coherence squared between the two modes in wavenumber-frequency space (shading in Fig. 4a). Within KWs (purple band), the coupling strength between the second baroclinic mode temperature and first baroclinic mode heating anomalies weakens within KWs (Fig. S6a). Meanwhile, the coupling strength between the first and second baroclinic modes (Fig. S6b) also weakens with warming (shading in Fig. S4a in this study and Fig. 11 in Chien and Kim (2024)[31]) and so does the coupling strength between the stratiform heating and the second baroclinic temperature (Fig. S6c, shading in Fig. S4c). These suggest that the two modes are strongly coupled within KWs in -4K, moderately coupled in CTL, and weakly coupled in +4K. This weakening of the coupling between the two modes implies that the KW dynamics change with warming.

In other words, as the surface warms, (i) the second baroclinic temperature anomalies are less efficient in generating deep convection, (ii) deep convective heating and stratiform heating are less correlated, and (iii) stratiform heating cannot effectively amplify the second mode temperature anomalies. Deep convective heating likely affects stratiform heating through the detrainment of hydrometers from deep convection to form stratiform clouds; stratiform heating likely affects the second baroclinic temperature anomalies through the eddy available potential energy (EAPE) generation, as mentioned in previous studies[15,20-22]. We speculate that the main reason that the coupling between the two modes weakens with warming is that the second baroclinic mode temperature anomalies are less effective in triggering deep convection as the surface warms. In the following, we focus on how the second baroclinic temperature affects deep convection. We hypothesize that the change in EOF2 structure is responsible for the change in coupling strength.

The change in coupling strength is important for KWs. Figure 4b shows the normalized power spectrum of precipitation anomalies (adapted from Chien and Kim 2024[32]), showing that KWs accelerate and weaken with warming. Within the KW band, the reduced precipitation power (Fig. 4b) is consistent with the reduced coupling strength (Fig. 4a). Based on detailed diagnostics of the maintenance and propagation mechanisms, the previous study associated the response of KWs with the weakening of coupling between the two modes[32], highlighting the importance of understanding the coupling process and why coupling weakens.

Over the past decades, different coupling mechanisms have been proposed in simple models that describe the destabilization of KWs within the second baroclinic mode component[20-22]. According to Mapes (2000)[22], cold anomalies in the lower troposphere from the second baroclinic structure decrease the static stability of the atmosphere and trigger deep convection. In Kuang (2008)[21], deep convection is triggered when the second baroclinic mode temperature perturbation changes from warm anomalies to cold anomalies in the lower troposphere. In Khouider and Majda (2006)[20], deep convection occurs when the midtroposphere is moist. By examining the phase relationship between these variables within KWs, we find that none of the above can fully explain the coupling mechanism in our simulations (a detailed comparison between our simulation results and previous simple models is described in Text S1). The next sections will provide some evidence of our proposed mechanism for how the change in EOF2 structure affects the coupling.

The coupling weakens due to the changes in the second baroclinic structure as the surface warms

Since we cannot fully explain coupling mechanisms (especially on how the second baroclinic mode temperature anomalies affect the first baroclinic mode diabatic heating anomalies) in our simulations based on previous simple models[20-22], we explore other possible coupling pathways. We first examine how the first baroclinic mode diabatic heating anomalies are correlated with temperature anomalies at each pressure level (Fig. S9b). We find that the first baroclinic mode diabatic heating and temperature anomalies are generally positively correlated in the upper troposphere and negatively correlated in the lower troposphere (Fig. S9b), resembling EOF2 (Fig. S9a), suggesting that deep convection – first baroclinic mode diabatic heating anomalies – tends to occur with the second baroclinic mode temperature perturbation. Among all pressure levels, the first baroclinic mode diabatic heating is most strongly correlated negatively with temperature in the lower troposphere between 600 and 800 hPa in all simulations. The negative correlation between deep convection and temperature in the lower troposphere is likely because deep convection favors a colder environment in the lower troposphere, as it is often associated with lower static stability. In -4K, deep convection is more sensitive to temperature in the lower levels, especially near 800 hPa, while in +4K, precipitation is more sensitive to temperature near 600 hPa. This suggests that deep convection is most sensitive to environmental stability at different vertical levels in different climates. Therefore, the second baroclinic mode temperature anomalies may not directly affect deep convection by modifying the stability (e.g., convective inhibition)[22,37] for the same pressure level in different climates.

On the other hand, in all climates, deep convection is sensitive to moisture for the same pressure level in the lower troposphere (750-850 hPa) (orange box in Fig. S10), suggesting that deep convection tends to occur when the lower troposphere is moist. While the above is true for anomalies in general, we also find that within KWs, the KW composite precipitation is roughly in phase with moisture in the lower troposphere (Fig. S11). Note that moisture budget analysis shows that moisture in the lower troposphere mainly comes from vertical advection of moisture (Fig. S12). Based on these, we suspect that the second baroclinic mode temperature anomalies may affect deep convection through vertical moisture advection in the lower troposphere. As the surface warms, the change in EOF2 structure may weaken lower tropospheric moisture advection, and thus, deep convection is weaker. In the following paragraphs, we will elaborate on details supporting the hypothesis that the change in the EOF2 structure weakens the coupling between the two modes within KWs.

Figure 5a synthesizes the coupling process between the two baroclinic modes within KWs in -4K, where the two modes are strongly coupled, and the KW amplitude is large. In the lower troposphere, the second baroclinic mode temperature anomalies (red and blue contours) present warm anomalies at the suppressed phase and cold anomalies at the enhanced phase. During the suppressed phase of precipitation (negative KW phase), warm anomalies in the lower troposphere increase stability below (red contours in Fig. 5a and Fig. S13b-left), and thus, the subgrid-scale convective updraft mass flux from the ZM deep convection scheme is suppressed (purple shading in Fig. S13b-left), which drives diabatic cooling around 800 hPa at KW phase -3π/4 (blue shading in Fig. 5a and Fig. S13a-left). Diabatic cooling anomalies are collocated with the grid-scale downward motion in the lower troposphere (arrows in Fig. 5a and Fig. S13a-left), suggesting that diabatic cooling enhances grid-scale downward motion, which is generally valid under the weak temperature gradient approximation[38,39]. As the downward motion weakens, the prevailing KW wind becomes easterly, which adds up to the mean state easterly (Fig. 1 in Chien and Kim 2024[32]) and thus enhances the surface latent heat flux, moistening the boundary layer between 850 to 950 hPa (Fig. S14-left). At this stage, moisture accumulates in the boundary layer (green contours in Fig. 5a).

As the KW phase evolves to a positive phase (i.e., stage of enhanced precipitation), the warm anomalies in the lower troposphere weaken (red contour in Fig. 5a and Fig. S13b-left), strengthening the sub-grid scale convective updraft mass from the ZM deep convection scheme (brown shading in Fig. S13b-left). The enhanced sub-grid scale convective updraft mass flux produces grid-scale diabatic heating around 800 hPa at KW phase π/4 (orange shading in Fig. 5a and Fig. S13a-left). Diabatic heating enhances grid-scale upward vertical velocity (arrows in Fig. 5a and Fig. S13a-left). As the large-scale upward motion strengthens, vertical moisture advection decreases moisture in the boundary layer (contours in Fig. S13c-left) and increases moisture in the lower troposphere (green contour in Fig. 5a). When moisture reaches a maximum in the lower troposphere, precipitation maximizes (at KW phase = π/2). After maximum precipitation, stratiform clouds develop and produce a dipole of heating anomalies (i.e., heating on top and cooling on the bottom), amplifying the initial second baroclinic mode temperature perturbation. Therefore, KWs are destabilized. The first and second baroclinic modes are tightly coupled in this climate state.

On the other hand, as the surface warms, KW amplitude is low, and the two modes are weakly coupled. Figure 5b shows that in +4K, this coupling mechanism is less efficient due to weaker temperature perturbations in the lower troposphere, which is related to the change in the second baroclinic mode's structure. The second baroclinic mode structure in +4K compared to that in -4K presents upward-shifted peaks and weaker variability right above the boundary layer (blue and red contours in Fig. 5b and Fig. S13b-right). A weaker temperature perturbation in the lower troposphere is less effective in perturbing stability, and thus, the sub-grid-scale updraft mass flux anomalies are weaker. Weaker sub-grid-scale updraft mass flux anomalies are associated with weaker grid-scale diabatic heating anomalies in the lower troposphere (shading in Fig. 5b and Fig. S13a-right), which are less effective in modulating the grid-scale vertical motions (arrows in Fig. 5b and Fig. S13a-right). Meanwhile, weaker vertical velocity leads to weaker moistening of the lower troposphere (shading in Fig. S13c-right) via vertical advection (contour in Fig. S13a-right and S10c-right). Reduced moisture anomalies in the lower troposphere (green contour in Fig. 5b) trigger weaker deep convection. Smaller stratiform heating with a larger phase lag follows deep convection (Fig. 7 in Chien and Kim 2024[32]). Weaker second baroclinic mode heating anomalies with a larger phase lag cannot effectively amplify the initial second-mode temperature perturbation in +4K. KW precipitation is damped in this climate state because the second and first baroclinic modes are weakly coupled.

A few parameters that summarize our proposed coupling mechanism are shown in Figure 6, displaying the relative amplitude of the normalized KW composite variables (quantified by the maximum and minimum of the anomalies of the normalized KW composite) in each simulation compared to those in the -4K simulation. In summary, the coupling process is that the second baroclinic mode temperature anomalies lower environmental stability and enhance the convective updraft in the lower troposphere from the ZM convection scheme before the onset of deep convection (Fig. 6a, b). The convective updraft mass flux enhances diabatic heating in the lower troposphere (Fig. 6c), which strengthens grid-scale upward motion (Fig. 6d). The lower tropospheric upward motion ahead of deep convection facilitates moistening of the lower troposphere via vertical advection (Fig. 6e). When the lower troposphere is moist (Fig. 6f), deep convection occurs. As the climate warms, the change in the EOF2 structure makes the second baroclinic mode heating less effective in generating temperature variability in the lower troposphere, which weakens static stability anomalies and the vertical velocity ahead of deep convection (Fig. 6a-d). Weaker vertical velocity is associated with weaker vertical advection of moisture (Fig. 6e), which weakens moisture in the lower troposphere (Fig. 6f), and thus deep convection weakens.

Combining all results, we conclude that as the surface warms, the coupling between the second baroclinic mode temperature and the first baroclinic mode heating weakens (i.e., the second baroclinic mode temperature anomalies are less effective in triggering deep convection) mainly due to the structural changes in EOF2 associated with the rise of the melting level. This weaker coupling leads to the weakening and acceleration of KWs[32]. Our results suggest that the response of KWs to surface warming is primarily affected by the melting level and the second baroclinic mode structure.

Discussion

While stratiform cloud processes are a crucial building block of tropical rainfall from mesoscale convective systems to planetary-scale tropical waves[1-4], how the stratiform heating structure would change in a warmer climate remains an open question. Despite the fact that convectively coupled Kelvin waves (KWs) are important drivers of extreme precipitation and flooding events in the tropics[40-43], few studies have focused on the changes of KWs with warming[30,32]. Further, the effect of changes in stratiform heating structure on KWs with surface warming remains unexplored.

This study analyzes the structural changes of stratiform heating structure and the response of KWs to surface temperature forcing using a set of three aquaplanet simulations with prescribed boundary conditions of sea surface temperature, representing the current climate (CTL), a 4K cooler (-4K) and a 4K warmer (+4K) climate. Results show that as the melting level rises (-2.7 %hPa/K) with warming, ice particles falling from the stratiform clouds melt at lower pressure levels. Thus, the stratiform heating structure presents upward-shifted peaks in the lower troposphere and weaker variability right on top of the boundary layer. The stratiform heating structure changes lead to weaker temperature variability, vertical motion, and moistening in the lower troposphere, which are less favorable for triggering deep convection. As a result, the coupling between stratiform heating and deep convection weakens within KWs, causing KWs to weaken (-4.7%/K) and accelerate (+7.1%/K) with warming. We propose a mechanism that connects the change in the mean state temperature profile with the interaction between clouds, which further impacts tropical waves. The findings of this study have further implications for understanding tropical climate change.

Our proposed mechanism of the coupling between deep convection (i.e., the first baroclinic mode) and the stratiform cloud processes (i.e., the second baroclinic mode) highlights that second baroclinic mode temperature anomalies affect deep convection by moistening the lower troposphere, which differs from the assumptions of previous simple models of the KWs[20-22]. Future studies can further examine this process in observations and other numerical models. Incorporating this process in simple models and examining their effect on KW growth and propagation would also be an interesting question. While our proposed coupling mechanism is based on the CAM6 simulations, it is necessary to verify this coupling process further in different numerical models and observations. Preliminary analysis of the observed KWs shows some similar moisture characteristics with the KWs in our simulations. Similarities include the in-phase relationship between KW precipitation and moisture in the lower troposphere, gradual moistening from the boundary layer to the lower troposphere, and vertical advection being the most dominant source of moisture in the lower troposphere (details are described in Text S2). However, more in-depth investigation of the coupling process within KWs in observation and other numerical simulations is needed.

It is worth mentioning that there is a discrepancy between the weakening of KWs with warming in our simulations and the strengthening of KWs in CMIP6 models[30]. While they speculated that the strengthening of KWs is associated with the increasing midlatitude wave activities, results from this study suggest it is also crucial to investigate the internal thermodynamic feedback between diabatic heating and temperature of KWs[23]. In particular, the change in the melting level and the second baroclinic mode structure, especially the location of the lower tropospheric peak of the second baroclinic structure. The location of the lower tropospheric peak would depend on the melting level and how efficiently the model cloud microphysics scheme treats melting processes. To what extent the second baroclinic mode structure affects lower tropospheric vertical velocity and moisture, as well as how precipitation interacts with the lower tropospheric moisture, could depend on the model physics, especially the cumulus parameterization of the model. The co-evolution of the second-mode temperature, moisture in the lower troposphere, and deep convection needs to be closely examined in CMIP6 models. Although the melting level is likely to rise in warmer climates, how it affects the KWs would depend on this co-evolution.

Meanwhile, recent global storm-resolving simulations show promising results in representing tropical waves[44]. Specifically targeting the KWs, recent studies showed that KW amplitude and growth are sensitive to convective parameterizations[45] and that KWs are stronger in convectively resolved simulations than in convectively parameterized simulations due to the differences in the vertical structure of diabatic heating[46]. Examining and comparing this co-evolution of temperature, moisture, and deep convection within KWs in convectively resolved and parameterized simulations would be interesting. Investigating this co-evolution would also provide insights into the future projections of KWs in storm-resolving simulations.

Methods

Aquaplanet simulations

Our study utilizes the sixth version of the Community Atmosphere Model (CAM6) to conduct aquaplanet simulations. Three sets of simulations are analyzed, with prescribed zonally symmetric sea surface temperature (SST), including the control simulation (CTL), the 4K cooler (-4K), and the 4K warmer (+4K) experiments. The simulation details are described by Chien and Kim (2024)[32]. Note that this study uses 3-year simulations for analyses.

KW diagnostic method

Our KW diagnostic includes meridional projection of all variables, space-time spectral analysis, composite field variables based on the convective phase of KWs, EOF analysis to obtain the vertical structure of the first and second baroclinic modes, and calculation of the eddy available potential energy (EAPE) growth rate associated with the two modes. Details of the above diagnostic are documented in Chien and Kim (2024)[32], summarized below: the meridional projection is adapted from previous studies[47-48], the space-time spectral analysis is adapted from the previous study that first designed this analysis[2], and the KW composite method is adapted from another study[49]. Note that because KW amplitude weakens with warming, it is reasonable that KW composite anomalies of all fields weaken with warming. To fairly compare the magnitude of KW composite anomalies in different simulations, all KW composite variables, except precipitation, are normalized by the KW amplitude of precipitation in each simulation. After normalization, the KW composite anomalies per unit of KW precipitation are shown. If not specified, the KW composite anomalies in this study represent the normalized version. Comparing the relative magnitude of the normalized anomalies provides more insights into how efficient precipitation or deep convection is generated in each simulation.

Acknowledgments

This study is based on MC's PhD dissertation. We appreciate Peter Blossey's feedback on improving the writing of this study. The aquaplanet simulations were performed based on high-performance computing resources from Cheyenne[50] and Derecho[51] provided by NCAR's Computational and Information Systems Laboratory, sponsored by the National Science Foundation. MC was supported by the PhD Fellowship from the Taiwanese Ministry of Science and Technology. DK was supported by the New Faculty Startup Fund from Seoul National University, the NASA MAP program (80NSSC21K1495), the NOAA MAPP program (NA21OAR4310343), and the NOAA CVP program (NA22OAR4310608).

Data availability

The aquaplanet simulation outputs for analysis are uploaded to GitHub using the following link: https://github.com/muting-chien/CCKW_coupling.

Code availability

The analysis code is also uploaded on GitHub using the following link: https://github.com/muting-chien/CCKW_coupling. The analysis codes are written primarily in functions, and therefore, they can be easily applied to analyze KWs in observations and other model simulations.

Author Contribution

MC performed simulations, completed all analyses and visualizations, and wrote the manuscript. DK provided additional ideas and interpretation and helped edit the manuscript.

Competing Interests

The authors declare no competing interests.

References

1.Mapes, B., Tulich, S., Lin, J., & Zuidema, P. (2006). The mesoscale convection life cycle: Building block or prototype for large-scale tropical waves?. *Dynamics of atmospheres and oceans*, *42*(1-4), 3-29, https://doi.org/10.1016/j.dynatmoce.2006.03.003

2. Wheeler, M., and G. N. Kiladis, (1999): Convectively coupled equatorial waves: Analysis of clouds and temperature in the wavenumber–frequency domain. *J. Atmos. Sci.*, 56, 374–399, https://doi.org/10.1175/1520-0469(1999)056,0374:CCEWAO.2.0.CO;2.

3. Madden, R. A., & Julian, P. R. (1971). Detection of a 40–50 day oscillation in the zonal wind in the tropical Pacific. *Journal of Atmospheric Sciences*, *28*(5), 702-708, https://doi.org/10.1175/1520-0469(1971)028<0702:DOADOI>2.0.CO;2

4. Madden, R. A., & Julian, P. R. (1972). Description of global-scale circulation cells in the tropics with a 40–50 day period. *Journal of Atmospheric Sciences*, *29*(6), 1109-1123, https://doi.org/10.1175/1520-0469(1972)029<1109:DOGSCC>2.0.CO;2

5. Schumacher, C., Houze Jr, R. A., & Kraucunas, I. (2004). The tropical dynamical response to latent heating estimates derived from the TRMM precipitation radar. *Journal of the Atmospheric Sciences*, *61*(12), 1341-1358, https://doi.org/10.1175/1520-0469(2004)061<1341:TTDRTL>2.0.CO;2

6. Houze Jr, R. A. (2004). Mesoscale convective systems. *Reviews of Geophysics*, *42*(4), **https://doi.org/10.1029/2004RG000150**

7. Trenberth, K. E., Stepaniak, D. P., & Caron, J. M. (2000). The global monsoon as seen through the divergent atmospheric circulation. *Journal of Climate*, *13*(22), 3969-3993, https://doi.org/10.1175/1520-0442(2000)013<3969:TGMAST>2.0.CO;2

8. Inoue, K., Adames, Á. F., & Yasunaga, K. (2020). Vertical Velocity Profiles in Convectively Coupled Equatorial Waves and MJO: New Diagnoses of Vertical Velocity Profiles in the Wavenumber–Frequency Domain. *Journal of the Atmospheric Sciences*, *77*(6), 2139-2162, https://doi.org/10.1175/JAS-D-19-0209.1

9. Chien, M. T., & Kim, D. (2023). Representation of the Convectively Coupled Kelvin Waves in Modern Reanalysis Products. *Journal of the Atmospheric Sciences*, *80*(2), 397-418, https://doi.org/10.1175/JAS-D-22-0067.1

10. Fulton, S. R., & Schubert, W. H. (1985). Vertical normal mode transforms: Theory and application. *Monthly Weather Review*, 113(4), 647-658.

11. Tulich, S. N., Randall, D. A., & Mapes, B. E. (2007). Vertical-mode and cloud decomposition of large-scale convectively coupled gravity waves in a two-dimensional cloud-resolving model. *Journal of the atmospheric sciences*, *64*(4), 1210-1229, https://doi.org/10.1175/JAS3884.1

12. Haertel, P. (2020). Kelvin/Rossby wave partition of Madden-Julian oscillation circulations. *Climate*, *9*(1), 2, **https://doi.org/10.3390/cli9010002**

13. Barnes, H. C., & Houze Jr, R. A. (2014). Precipitation hydrometeor type relative to the mesoscale airflow in mature oceanic deep convection of the Madden-Julian Oscillation. *Journal of Geophysical Research: Atmospheres*, *119*(24), 13-990, **https://doi.org/10.1002/2014JD022241**

14. Barnes, H. C., & Houze Jr, R. A. (2016). Comparison of observed and simulated spatial patterns of ice microphysical processes in tropical oceanic mesoscale convective systems. *Journal of Geophysical Research: Atmospheres*, *121*(14), 8269-8296, **https://doi.org/10.1002/2014JD022241**

15. Straub, K. H, G. N. Kiladis, 2003: The observed structure of convectively coupled Kelvin waves: Comparison with simple models of coupled wave instability. *J. Atmos. Sci.*, 60, 1655–1668, https://doi.org/10.1175/1520-0469(2003)060,1655:TOSOCC.2.0.CO;2.

16. Kiladis, G. N., Wheeler, M. C., Haertel, P. T., Straub, K. H., & Roundy, P. E. (2009). Convectively coupled equatorial waves. *Reviews of Geophysics*, *47*(2), https://doi.org/10.1029/2008RG000266

17. Lindzen, R. S., 1974: Wave-CISK in the tropics. *J. Atmos. Sci.*, 31, 156–179, https://doi.org/10.1175/1520-0469(1974)031,0156:WCITT.2.0.CO;2.

18. Emanuel, K. A., 1987: An air-sea interaction model of intraseasonal oscillations in the tropics. *J. Atmos. Sci.*, 44, 2324–2340, https://doi.org/10.1175/1520-0469(1987)044,2324:AASIMO.2.0.CO;2.

19. Raymond, D. J., and Zˇ . Fuchs, 2007: Convectively coupled gravity and moisture modes in a simple atmospheric model. *Tellus*, 59A, 627–640, https://doi.org/10.1111/j.1600-0870.2007.00268.x.

20. Khouider, B., & Majda, A. J. (2006). A simple multicloud parameterization for convectively coupled tropical waves. Part I: Linear analysis. *Journal of the atmospheric sciences*, *63*(4), 1308-1323, https://doi.org/10.1175/JAS3677.1

21. Kuang, Z., 2008: A moisture-stratiform instability for convectively coupled waves. *J. Atmos. Sci.*, 65, 834–854, https://doi.org/10.1175/2007JAS2444.1.

22. Mapes, B. E., 2000: Convective inhibition, subgrid-scale triggering energy, and stratiform instability in a toy tropical wave model. *J. Atmos. Sci.*, 57, 1515–1535, https://doi.org/10.1175/1520-469(2000)057,1515:CISSTE.2.0.CO;2.

23. Chien, M. T., Kim, D., and Haertel, P. (2025). Maintenance of convectively coupled Kelvin waves: relative importance of internal thermodynamic feedback and external momentum forcing. *EarthArxiv*

24. Ma, J., Xie, S. P., & Kosaka, Y. (2012). Mechanisms for tropical tropospheric circulation change in response to global warming. *Journal of Climate*, *25*(8), 2979-2994, https://doi.org/10.1175/JCLI-D-11-00048.1

25. Folkins, I. (2013). The melting level stability anomaly in the tropics. *Atmospheric Chemistry and Physics*, *13*(3), 1167-1176, https://doi.org/10.5194/acp-13-1167-2013

26. Vallis, G. K., Zurita-Gotor, P., Cairns, C., & Kidston, J. (2015). Response of the large-scale structure of the atmosphere to global warming. *Quarterly Journal of the Royal Meteorological Society*, *141*(690), 1479-1501, **https://doi.org/10.1002/qj.2466**

27. O'Gorman, P. A., & Singh, M. S. (2013). Vertical structure of warming consistent with an upward shift in the middle and upper troposphere. *Geophysical research letters*, *40*(9), 1838-1842, **https://doi.org/10.1002/grl.50328**

28. Singh, M. S., & O'Gorman, P. A. (2012). Upward shift of the atmospheric general circulation under global warming: Theory and simulations. *Journal of Climate*, *25*(23), 8259-8276, https://doi.org/10.1175/JCLI-D-11-00699.1

29. Prein, A. F., & Heymsfield, A. J. (2020). Increased melting level height impacts surface precipitation phase and intensity. *Nature Climate Change*, *10*(8), 771-776, https://doi.org/10.1038/s41558-020-0825-x

30. Bartana, H., Garfinkel, C. I., Shamir, O., & Rao, J. (2022). Projected future changes in equatorial wave spectrum in CMIP6. *Climate Dynamics*, 1-13, https://doi.org/10.1007/s00382-022-06510-y

31. Eyring, Veronika, Bony, Sandrine, Meehl, Gerald A., Senior, Catherine A., Stevens, Bjorn, Stouffer, Ronald J., Taylor, Karl E., 2016: Overview of the Coupled Model Intercomparison Project Phase 6 (CMIP6) experimental design and organization. *Geoscientific Model Development*, **9**, 1937-1958, doi:10.5194/gmd-9-1937-2016.

32. Chien, M. T., & Kim, D. (2024). Response of convectively coupled Kelvin waves to surface temperature forcing in aquaplanet simulations. *Journal of Advances in Modeling Earth Systems*, 16(10), e2024MS004378, https://doi.org/10.1029/2024MS004378

33. Zhang, G. J., & McFarlane, N. A. (1995). Role of convective scale momentum transport in climate simulation. *Journal of Geophysical Research: Atmospheres*, *100*(D1), 1417-1426, https://doi.org/10.1029/94JD02519

34. Golaz, J. C., Larson, V. E., & Cotton, W. R. (2002). A PDF-based model for boundary layer clouds. Part I: Method and model description. *Journal of the atmospheric sciences*, *59*(24), 3540-3551, https://doi.org/10.1175/1520-0469(2002)059<3540:APBMFB>2.0.CO;2

35. Bogenschutz, P. A., Gettelman, A., Morrison, H., Larson, V. E., Craig, C., & Schanen, D. P. (2013). Higher-order turbulence closure and its impact on climate simulations in the Community Atmosphere Model. *Journal of Climate*, *26*(23), 9655-9676, https://doi.org/10.1175/JCLI-D-13-00075.1

36. Gettelman, A., & Morrison, H. (2015). Advanced two-moment bulk microphysics for global models. Part I: Off-line tests and comparison with other schemes. *Journal of Climate*, *28*(3), 1268-1287, https://doi.org/10.1175/JCLI-D-14-00102.1

37. Weber, N. J., Kim, D., & Mass, C. F. (2021). Convection–Kelvin wave coupling in a global convection-permitting model. *Journal of the Atmospheric Sciences*, *78*(4), 1039-1055, https://doi.org/10.1175/JAS-D-20-0243.1

38. Charney, J. G., 1963: A note on large-scale motions in the tropics. *J. Atmos. Sci.*, **20**, 607–609.

39. Sobel, A. H., Nilsson, J., & Polvani, L. M. (2001). The weak temperature gradient approximation and balanced tropical moisture waves. Journal of the atmospheric sciences, 58(23), 3650-3665, https://doi.org/10.1175/1520-0469(2001)058<3650:TWTGAA>2.0.CO;2

40. Chen, W. T., Hsu, S. P., Tsai, Y. H., & Sui, C. H. (2019). The influences of convectively coupled Kelvin waves on multiscale rainfall variability over the South China Sea and Maritime Continent in December 2016. *Journal of Climate*, 32(20), 6977-6993. https://doi.org/10.1175/JCLI-D-18-0471.1

41. Latos, B., Lefort, T., Flatau, M. K., Flatau, P. J., Permana, D. S., Baranowski, D. B., ... & Schmidt, J. M. (2021). Equatorial waves triggering extreme rainfall and floods in southwest Sulawesi, Indonesia. *Monthly Weather Review*, *149*(5), 1381-1401, https://doi.org/10.1175/MWR-D-20-0262.1

42. Peyrillé, P., Roehrig, R., & Sanogo, S. (2023). Tropical waves are key drivers of extreme precipitation events in the Central Sahel. *Geophysical Research Letters*, *50*(20), e2023GL103715, https://doi.org/10.1175/MWR-D-20-0262.1

43. Cheng, Y. M., Dias, J., Kiladis, G., Feng, Z., & Leung, L. R. (2023). Mesoscale convective systems modulated by convectively coupled equatorial waves. *Geophysical Research Letters*, *50*(10), e2023GL103335, **https://doi.org/10.1029/2023GL103335**

44. Judt, F., & Rios-Berrios, R. (2021). Resolved convection improves the representation of equatorial waves and tropical rainfall variability in a global nonhydrostatic model. *Geophysical Research Letters*, 48(14), e2021GL093265, **https://doi.org/10.1029/2021GL093265**

45. Lee, S.-H., Park, S.-H., Chien, M.-T., & Kim, D. (2025). Simulations of Convectively Coupled Kelvin Waves (CCKWs) with Three Different Cumulus Parameterization Schemes. *Journal of Geophysical Research – Atmosphere*, https://doi.org/10.1029/2024JD042738

46. Rios-Berrios, R., Judt, F., Bryan, G., Medeiros, B., & Wang, W. (2023). Three-dimensional structure of convectively coupled equatorial waves in aquaplanet experiments with resolved or parameterized convection. *Journal of Climate*, 36(9), 2895-2915, https://doi.org/10.1175/JCLI-D-22-0422.1

47. Cheng, Y. M., Tulich, S., Kiladis, G. N., & Dias, J. (2022). Two extratropical pathways to forcing tropical convective disturbances. *Journal of Climate*, *35*(20), 2987-3009, https://doi.org/10.1175/JCLI-D-22-0171.1

48. Tulich, S. N., & Kiladis, G. N. (2021). On the regionality of moist Kelvin waves and the MJO: The critical role of the background zonal flow. *Journal of Advances in Modeling Earth Systems*, *13*(9), e2021MS002528, https://doi.org/10.1029/2021MS002528

49. Nakamura, Y., & Takayabu, Y. N. (2022). Convective Couplings with Equatorial Rossby Waves and Equatorial Kelvin Waves. Part I: Coupled Wave Structures. *Journal of the Atmospheric Sciences*, *79*(1), 247-262, https://doi.org/10.1175/JAS-D-21-0080.1

50. Computational and Information Systems Laboratory. (2019). Cheyenne: HPE/SGI ICE XA System (University Community Computing). Boulder, CO: National Center for Atmospheric Research. https://doi.org/10.5065/D6RX99HX.

51. Computational and Information Systems Laboratory. (2024). Derecho: HPE Cray EX System (University Community Computing). Boulder, CO: National Center for Atmospheric Research. https://doi.org/10.5065/qx9a-pg09.

Figures

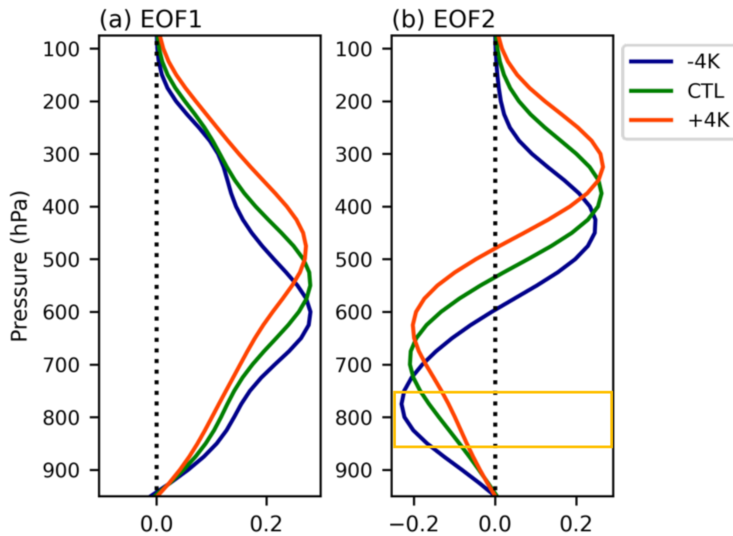

Figure 1. Vertical profile of (a) the first and (b) the second EOF structure of diabatic heating. The orange square marks the lower troposphere (750-850 hPa).

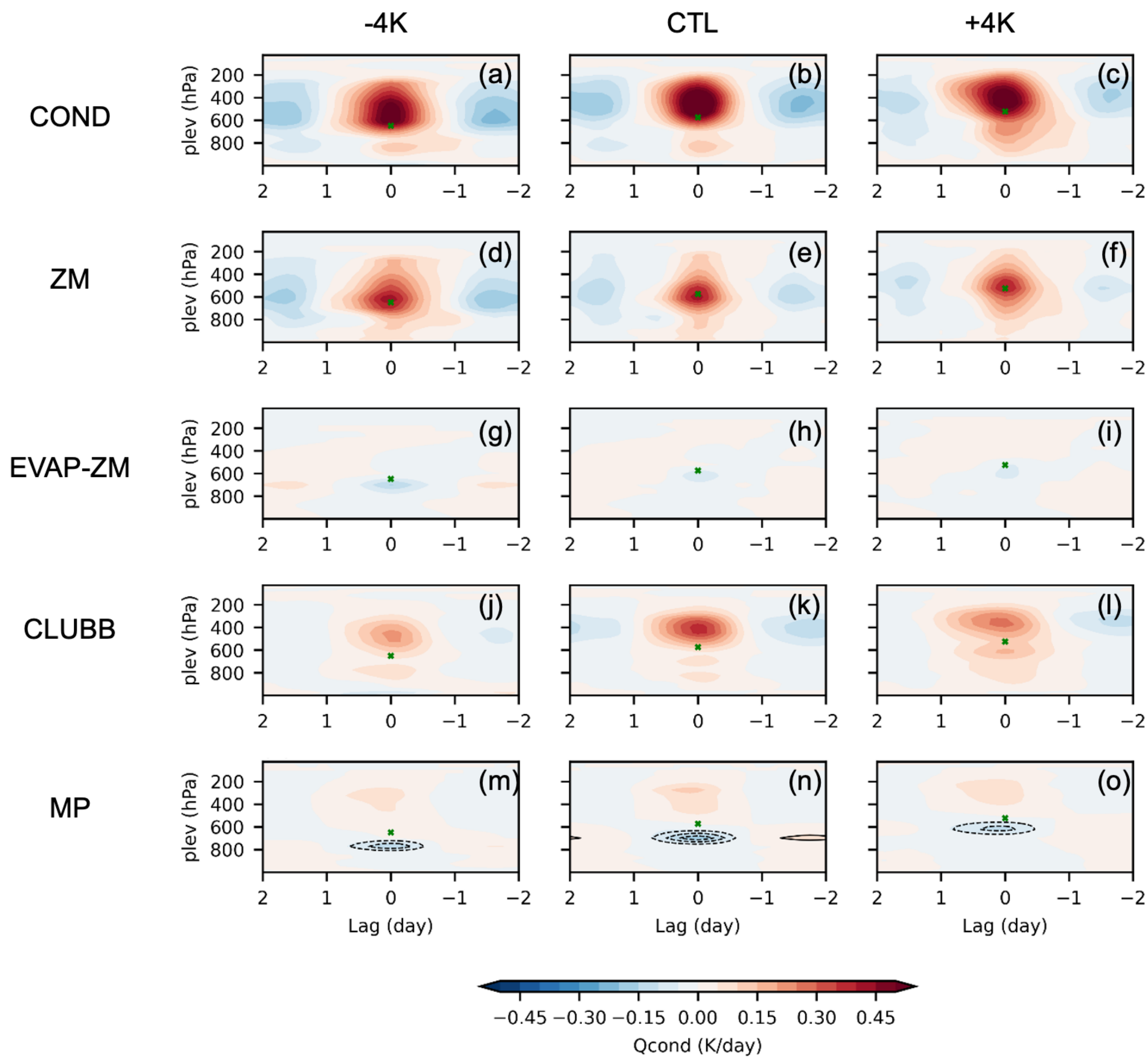

Figure 2. Lag regression of temperature tendency upon raw precipitation anomalies for each physical process: (a-c) total condensation, (d-f) ZM scheme, (g-i) evaporation from ZM scheme, (j-l) CLUBB, and (m-o) microphysics scheme. Note that latent heat from melting is shown in contours on (m-o). This regression is normalized by the variance of precipitation anomalies in each experiment, representing the temperature tendency per precipitation unit. The x-axis in each panel is flipped to be comparable to the KW composite figures shown earlier. The melting levels for each experiment are indicated in green crosses.

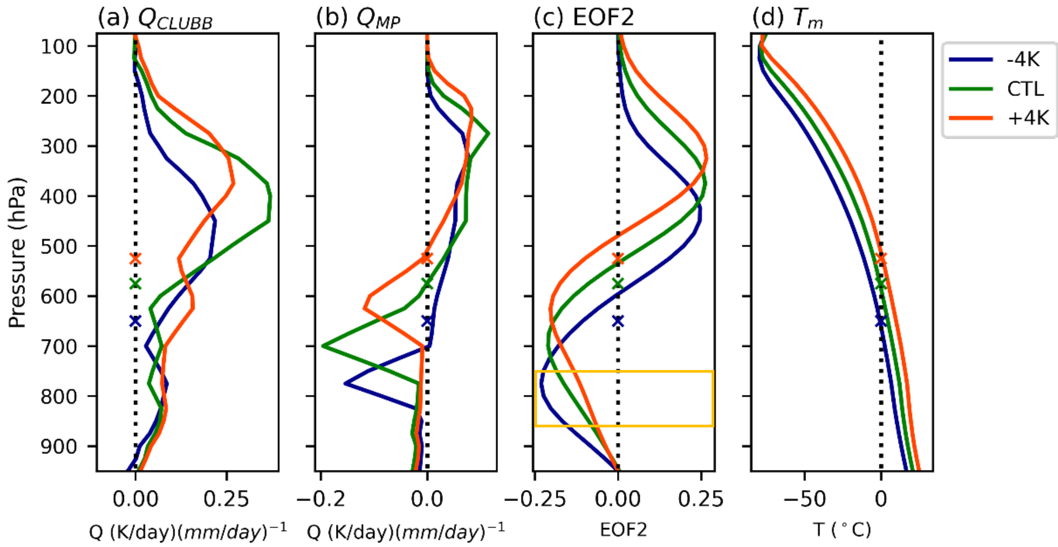

Figure 3. Vertical profile of (a) diabatic heating from CLUBB scheme regressed upon precipitation anomalies at lag day 0, (b) diabatic heating from microphysics scheme regressed upon precipitation anomalies at lag day 0, and (c) the second EOF structure of diabatic heating. Melting levels for each experiment are indicated in crosses, and (d) mean state temperature averaged within 10˚S-10˚N. Melting levels for each experiment are indicated in crosses. The orange square marks the lower troposphere (750-850 hPa).

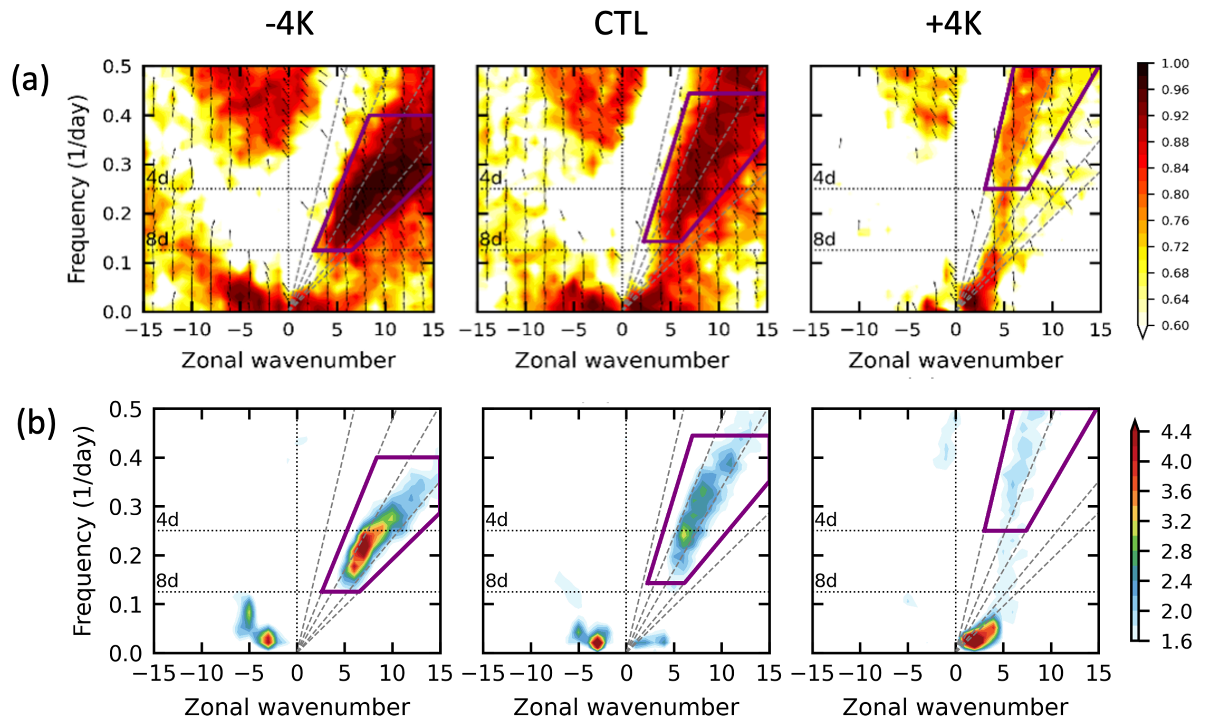

Figure 4. (a) Coherence squared (shading) and phase-relationship (arrows) between the second mode temperature (T2) and the first mode heating (Q1) anomalies in wavenumber-frequency space. KW band is indicated in purple polygons. Arrows pointing leftward (rightward) represent the latter variable lags (leads) the former variable; arrows pointing upward (downward) represent that the two variables are in phase (out of phase). (b) Normalized power spectrum of the equatorially symmetric component of precipitation anomalies over 10S-10N, adapted from Chien and Kim (2024). The grey slanted dashed lines represent different equivalent depths, which are 8, 12, 25, 50, and 150 m counterclockwise. The horizontal dotted lines indicate 4-day and 8-day.

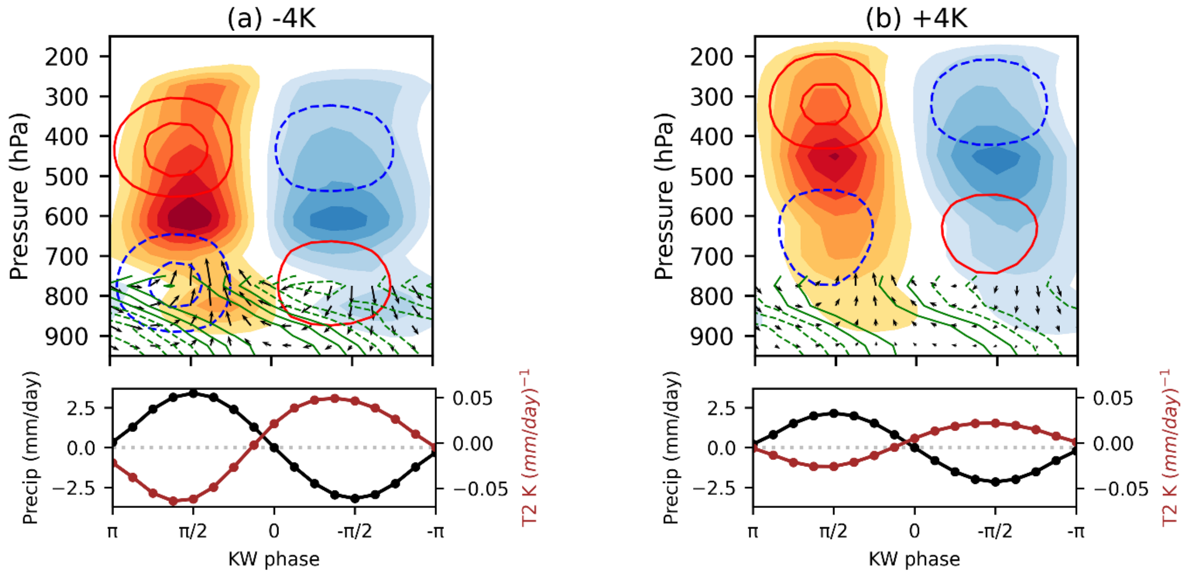

Figure 5. (Top panel) KW composite diabatic heating anomalies (shading), second baroclinic temperature anomalies (red and blue contours), specific humidity anomalies in the lower troposphere (green contours), and zonal and vertical wind anomalies in the lower troposphere (arrows) in (a) -4K and (b) +4K. These summarize the coupling process between the two modes. (Bottom panel) Black lines indicate KW composite precipitation (y-axis on the left), and brown lines indicate the second baroclinic mode temperature anomalies (y-axis on the right).

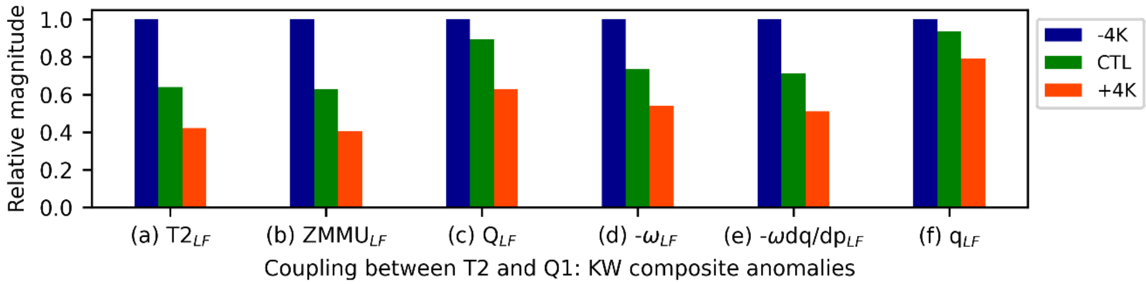

Figure 6. The relative amplitude of the normalized KW composite anomalies averaged in the lower troposphere (750-850 hPa): (a) the second baroclinic mode temperature, (b) convective updraft mass flux from the ZM deep convection scheme, (c) diabatic heating, (d) vertical pressure velocity, (e) vertical advection of moisture, and (f) specific humidity. The relative amplitude is the amplitude of each variable compared to those in -4K simulations.

Npj Climate and Atmospheric Science

Supporting Information for

Changes in stratiform heating structure due to surface warming weaken and accelerate convectively coupled Kelvin waves

Mu-Ting Chien[a] and Daehyun Kim[b,c]

[a]Department of Atmospheric Science, Colorado State University

[b]School of Earth and Environmental Sciences, Seoul National University, South Korea

[c]Department of Atmospheric and Climate Science, University of Washington

Contents of this file

Text S1 to S3
Figures S1 to S19

Introduction

The supporting information contains six figures that are supplementary to the main results.

Text S1. Comparison of the coupling process in our simulations with previous linear models of KWs

Different coupling mechanisms have been proposed in simple models that describe the destabilization of KWs within the second baroclinic mode component (e.g., Mapes 2000; Kuang 2008; Khouider and Majda 2006). Figure S6 summarizes critical steps that are common to all models above: (a) the second baroclinic mode temperature perturbation triggers deep convection (also known as the first baroclinic mode heating) (T2 to Q1), (b) deep convection affects second baroclinic mode heating (Q1 to Q2), and (c) the second baroclinic mode heating amplifies the second baroclinic mode temperature (Q2 to T2). Note that precipitation is mainly driven by deep convection; thus, maximum precipitation occurs when deep convection is strongest. In the later paragraphs, precipitation and deep convection are used interchangeably.

In Mapes (2000), convective inhibition (CIN) is crucial for the coupling. That is, the lower tropospheric cold anomalies from the second baroclinic mode temperature perturbation correspond to low CIN and trigger deep convection (T2 to Q1). Stratiform clouds develop three hours after deep convection and produce a heating-over-cooling pattern (Q1 to Q2). The heating-over-cooling pattern amplifies the second baroclinic mode temperature perturbation (Q2 to T2). If this mechanism is at work, deep convection would occur simultaneously with minimum CIN. To test this mechanism, we calculate deep convective inhibition (DCIN), an indicator of the environmental stability for convection originating within the boundary layer. The calculation of DCIN is adapted from Fuchs et al. (2014) and Weber et al. (2021):

$$\text{DCIN} = MSE_t^* \text{-} MSE_{bl}, \tag{1}$$

where MSE_{bl} is the moist static energy within the boundary layer (below 900hPa, determined based on the layers with nearly constant potential temperature), and MSE_t^* is the minimum saturated moist static energy above the boundary layer (825 hPa for -4K and 850 hPa for CTL and +4K). DCIN is qualitatively similar to CIN in Mapes (2000). We find that maximum KW precipitation (Fig. S8a) and minimum DCIN present a substantial phase lag (2/8-3/8 π) (Fig. S8c), suggesting that the coupling mechanism in our simulations cannot be fully explained by that in Mapes (2000).

In a later model by Kuang (2008), deep convection is in quasi-equilibrium with the tropospheric temperature within the second baroclinic component. In other words, the change in second-mode temperature perturbation triggers deep convection (T2 to Q1). Deep convection moistens the midtroposphere and helps the development of stratiform clouds (Q1 to Q2). The stratiform heating and cooling amplify the second baroclinic mode temperature perturbation (Q2 to T2). If this mechanism works in our simulations, deep convection would be in quadrature with the second baroclinic mode temperature perturbation (out-of-phase with the second baroclinic mode temperature tendency). However, in our simulations, precipitation is roughly out-of-phase with the second baroclinic mode temperature perturbation (Fig. S8d), suggesting that the coupling mechanism in our simulations cannot be fully explained by Kuang (2008) either.

In another model from Khouider and Madja (2006), the coupling mechanism is complicated because deep convection is parameterized based on confounding factors in the boundary layer and the free troposphere. The coupling mechanism is described as follows: Start with the second baroclinic mode temperature perturbation and its associated zonal wind. The second baroclinic mode zonal wind convergence in the lower troposphere moistens the midtroposphere. When the midtroposphere is dry, congestus clouds continue to develop and keep moistening the midtroposphere. When the midtroposphere is moist, precipitation occurs (T2 to Q1). Precipitation is enhanced when the lower troposphere is cold and the boundary layer is warm and moist. Stratiform heating appears after precipitation with a time lag of three hours (Q1 to Q2). The stratiform and congestus heating amplifies the second baroclinic mode temperature perturbation and the associated zonal wind perturbation (Q2 to T2). In our simulations, precipitation is roughly in-phase with the lower tropospheric moisture anomalies (Fig. S8b) instead of the midtropopheric moisture, suggesting that the coupling mechanism in our simulations cannot be fully explained by Khouider and Majda (2006) either.

Text S2: Moisture diagnostics of the observed KWs

Text S2 compares the moisture diagnostics in the observed KWs with those in our simulations. The observed KWs are obtained from the satellite observed 3-hourly ERA5 reanalysis and the cloud brightness temperature data from the CLAUS dataset from 1998 to 2013. For simplicity, we use the term "observation" to represent the combined results from CLAUS and ERA5. Figure S15 shows that the first baroclinic mode diabatic heating anomalies are also most strongly correlated with moisture in the lower troposphere in observation. However, the pressure levels with the highest correlation in observation are around 650-750 hPa, while those with the highest correlation in our simulations are around 750-850 hPa. Figure S16 shows that vertical advection of moisture is also the dominant source of moisture in observation. Figure S14 shows the KW composite moisture tendency (shading) and the vertical advection of moisture (contour). In the observed KWs (Fig. S17d), moisture also accumulates in the boundary layer first and then the lower troposphere, although the moistening is more rapid than that in aquaplanet simulations (Fig. S17a-c). Moistening in the lower troposphere in the observed KWs is also positively correlated with vertical advection of moisture ahead of deep convection. This suggests that the gradual moistening in the lower troposphere ahead of deep convection, a key component of our proposed coupling mechanism, is likely valid in the observed KWs. Future studies can more deeply diagnose the moisture evolution of the observed KWs and compare that with the proposed mechanism in our simulations.

Text S3. Vertical-shift transformation of temperature

The vertical-shift transformation of temperature is used to explain the vertical profile of temperature change with warming, originated from Singh and O'Gorman (2012) and O'Gorman and Singh (2013). They found that temperature change for each pressure level can be calculated as follows:

$$\Delta T_{VST}(p) = (\beta - 1)\left(p\frac{\partial T}{\partial p} - \frac{R_v T^2}{L}\right),$$

where T represents temperature, β is a constant, R_v is the gas constant for water vapor, and L is the latent heat of vaporization and sublimation of water. β is obtained from fitting the actual temperature change from CTL to +4K (-4K) simulations at the boundary layer top (850 hPa). The boundary layer top is used for fitting as it is the lowest level that would satisfy vertical-shift transformation. This is because the temperature change within the boundary layer could be affected by surface processes and mixing and thus are more complicated than vertical shift.

The physical interpretation of this equation is that the first term represents the vertical shift of temperature, and the second term represents the additional effect of latent heat due to the vertical shift of specific humidity and relative humidity.

By applying our simulated temperature profile from CTL and the fitted parameter β from CTL to +4K (-4K) to the above equation, we obtain the vertical shift of temperature in our simulations in Fig. S4.

Figure S4 shows that there is a thick layer of roughly constant warming between 500 and 700 hPa. That thick layer of roughly constant warming is due to the cancellation of (1) slightly decreases of the first term as pressure decreases (because of the increase of static stability ($\frac{\partial T}{\partial p}$) canceled by the pressure level (p) itself) and (2) the slight increase of the second negative term as the pressure decreases (because of the decrease in mean state temperature as pressure decreases, the cooling effect of saturation moisture decreases as pressure decreases) (Fig. S18). Note that the kink of VST around 800 hPa is due to the kink in the static stability profile in CTL (Fig. S19).

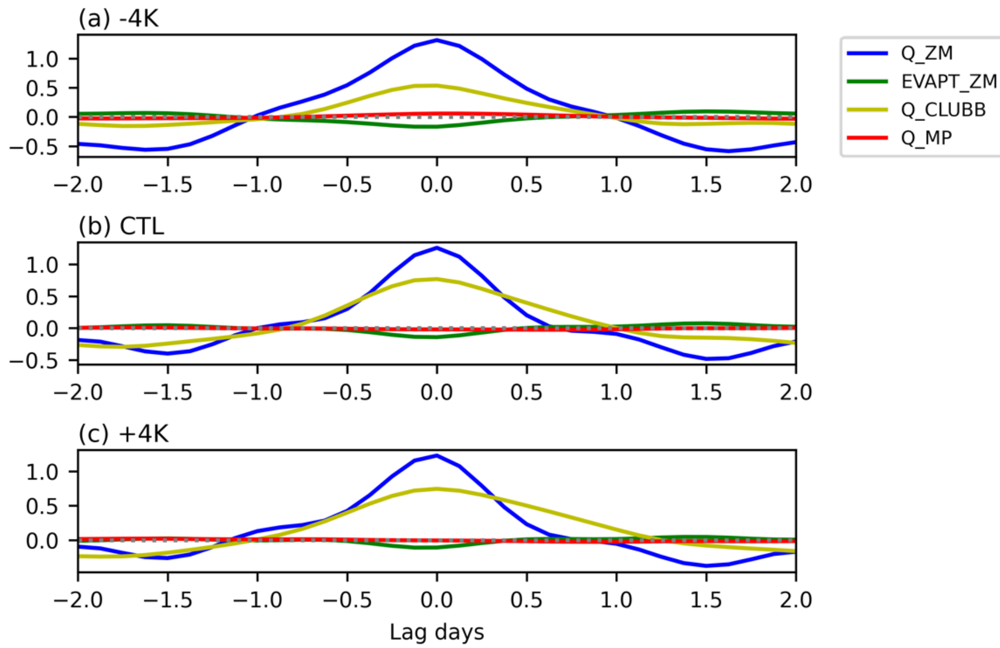

Figure S1. Contribution of each temperature tendency term to EOF1. The extent of the y-axis changes in each panel to best represent the relative importance of each process in each simulation.

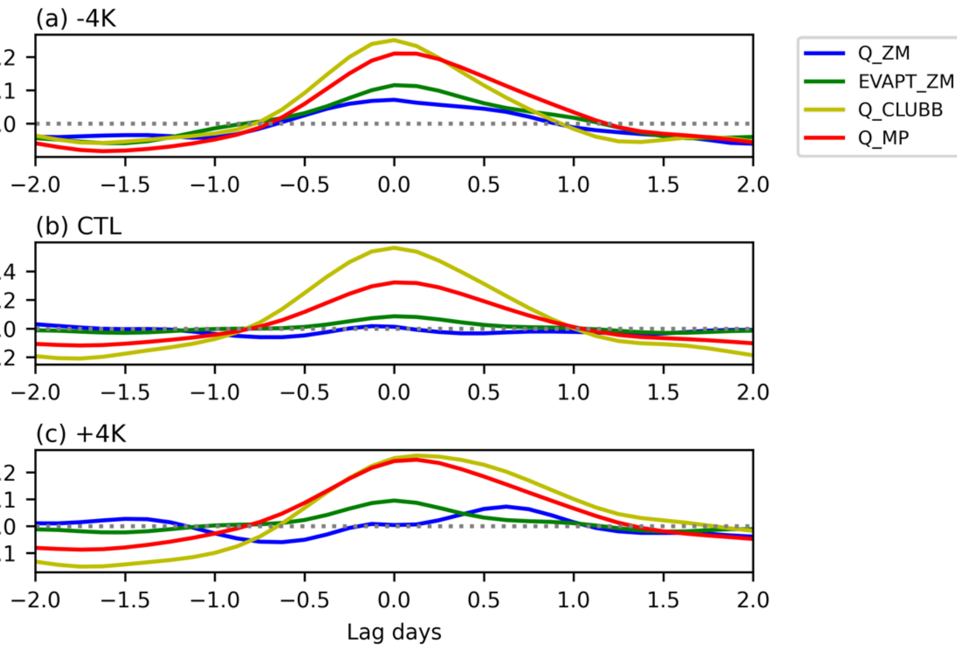

Figure S2. Similar to Fig. S1, but for EOF2.

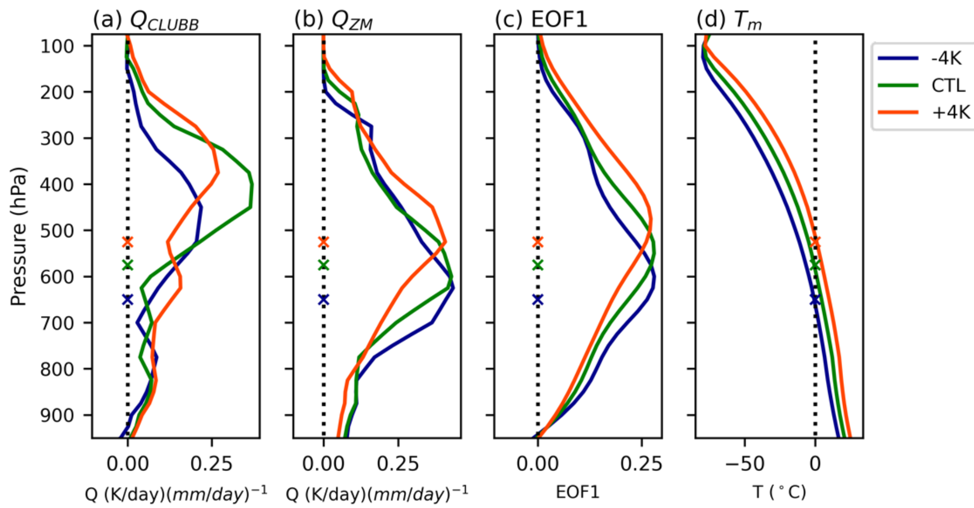

Figure S3. Vertical profile of (a) diabatic heating from CLUBB scheme regressed upon precipitation anomalies at lag day 0, (b) diabatic heating from ZM deep convection scheme regressed upon precipitation anomalies at lag day 0, and (c) the first EOF structure of diabatic heating. Melting levels for each experiment are indicated in crosses, and (d) mean state temperature averaged within 10˚S-10˚N. Melting levels for each experiment are indicated in crosses. The orange square marks the lower troposphere (750-850 hPa).

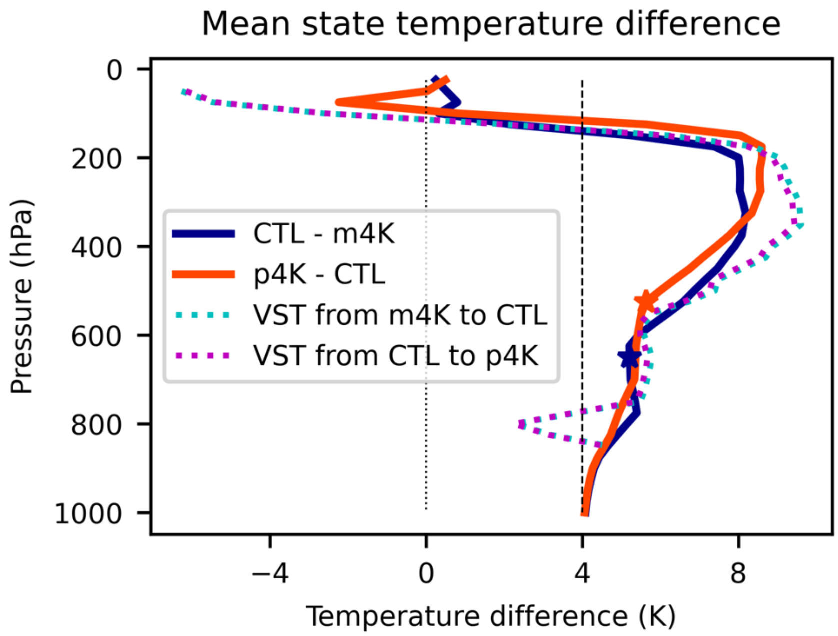

Figure S4. The tropical (10˚S-10˚N) mean state temperature difference between (1) CTL and warming (+4K, labeled as p4K in this figure) experiments, shown in red solid line, and (2) CTL and cooling (-4K, labeled as m4K in this figure) experiments, shown in dark blue solid line. Dashed lines represent theoretical temperature differences calculated from the vertical structure transform (VST) based on O'Gorman and Singh (2013). The dashed cyan line represents the temperature difference from -4K to CTL calculated from VST; the dashed magenta line represents the temperature difference from CTL to +4K calculated from VST.

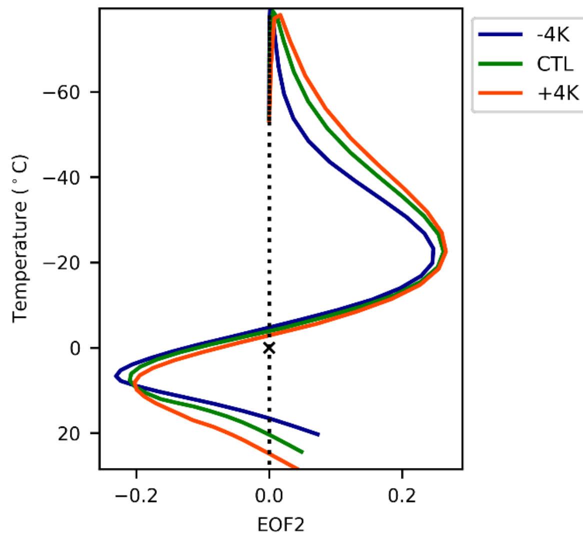

Figure S5. The vertical structure of the second baroclinic mode as a function of the mean state temperature averaged over the tropics (10S-10N). Black cross indicates the melting level.

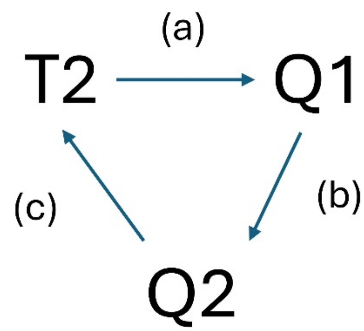

Figure S6. Illustration of the interaction between second mode temperature (T2), first mod heating (Q1), and second mode heating (Q2).

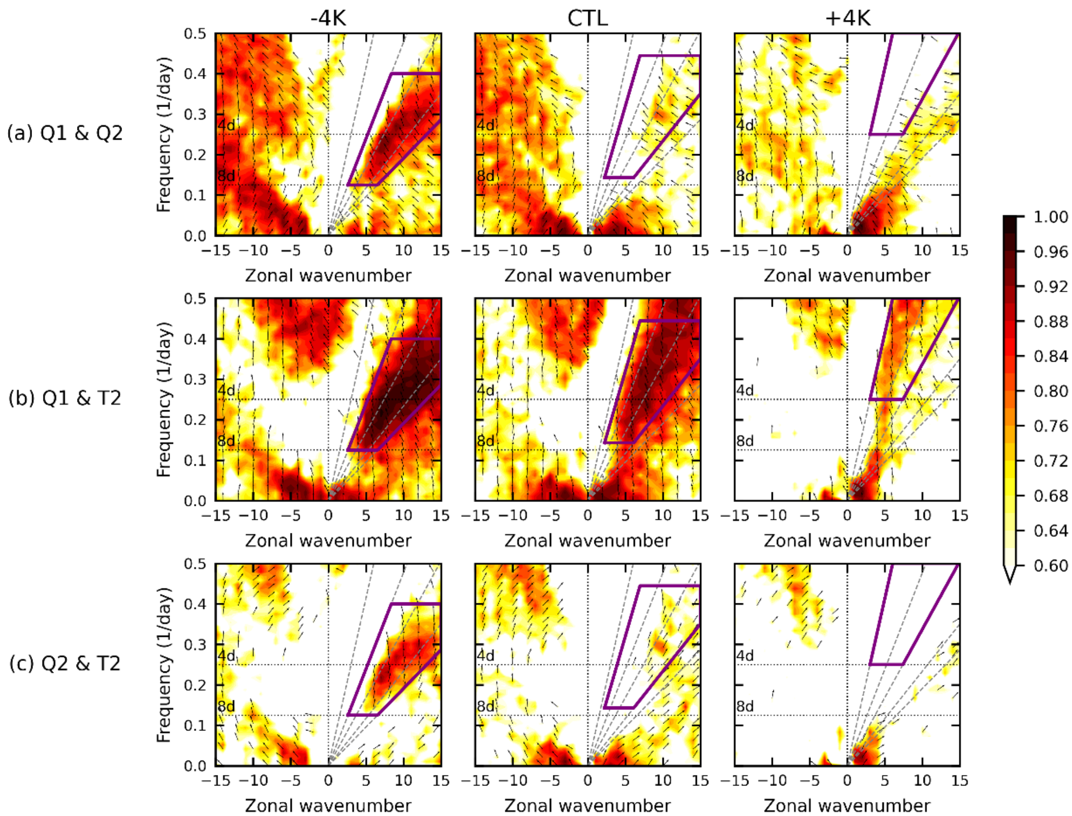

Figure S7. Coherence squared (shading) and phase-relationship (arrows) between (a) the first and second baroclinic mode heating anomalies (Q1 and Q2), (b) the second mode temperature (T2) and the first mode heating (Q1) anomalies, and (c) the second mode heating (Q2) and temperature (T2) anomalies in wavenumber-frequency space. KW band is indicated in purple polygons. (a) is similar to Fig. 11 in Chien and Kim (2024), except that only 3-year of data is used here to be consistent with other analyses in this paper. Arrows pointing leftward (rightward) represent the latter variable lagging (leading) the former variable; arrows pointing upward (downward) represent the two variables are in phase (out of phase).

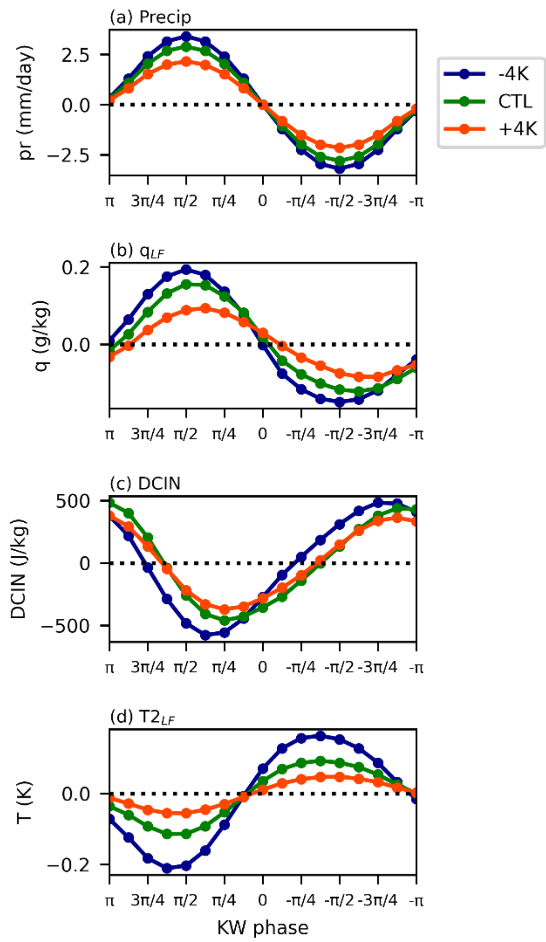

Figure S8. KW composite (a) precipitation, (b) lower tropospheric specific humidity (750-850 hPa), (c) deep convective inhibition (lower tropospheric saturation moist static energy - boundary layer moist static energy), (d) lower tropospheric temperature perturbation of the second baroclinic component (750-850 hPa).

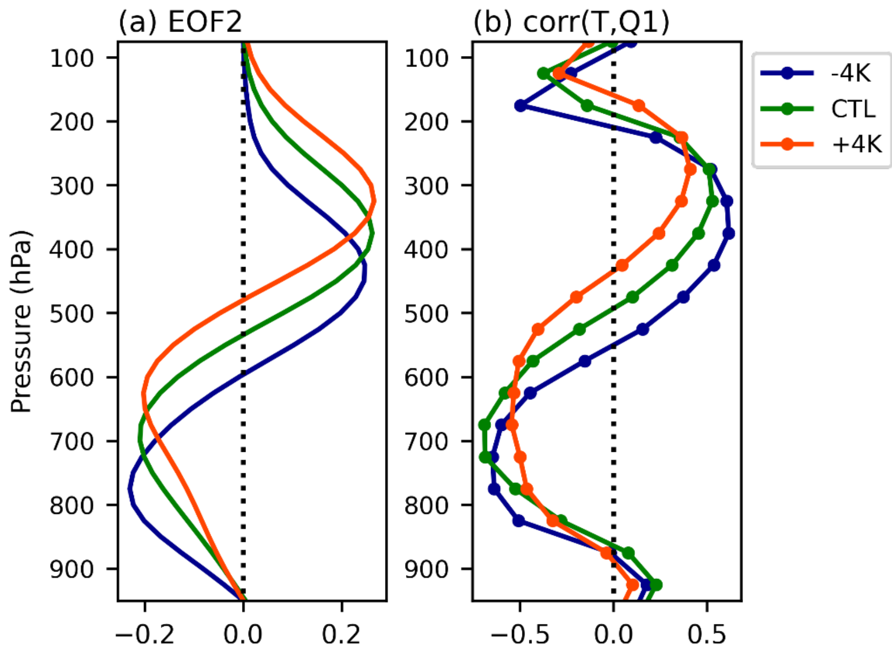

Figure S9. (a) Vertical profile of the second EOF of diabatic heating. (b) The correlation coefficient between the first baroclinic mode heating and temperature anomalies for each pressure level for surface warming experiments.

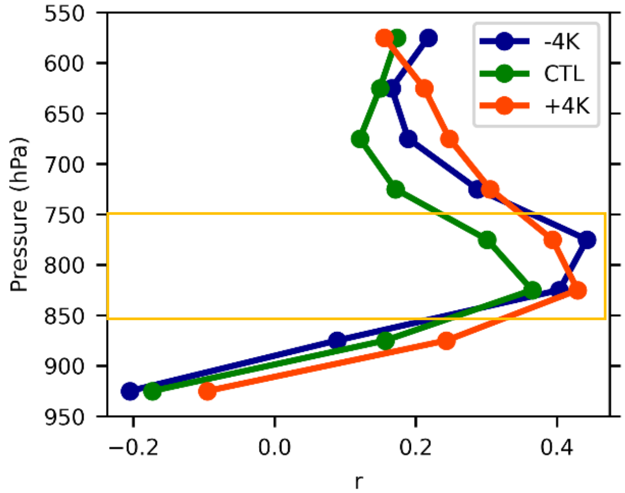

Figure S10. The correlation coefficient between first mode diabatic heating and specific humidity anomalies for each pressure level for surface warming experiments. Orange square marks the lower troposphere (750 to 850 hPa), where correlation is strongest.

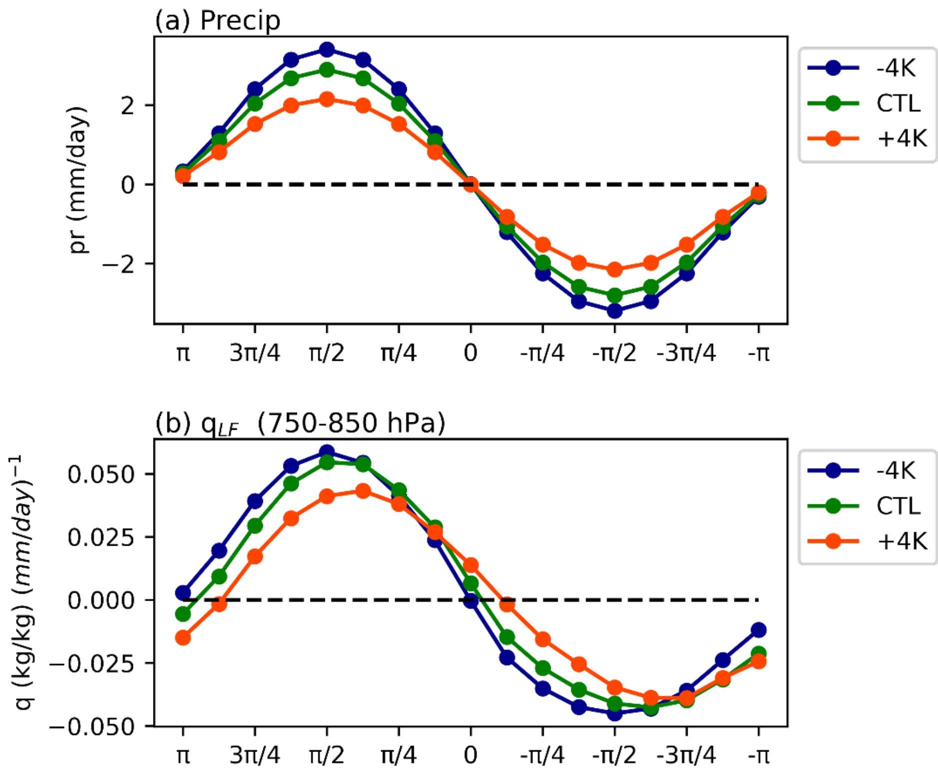

Figure S11. KW composite (a) precipitation, (b) normalized specific humidity in the lower free troposphere.

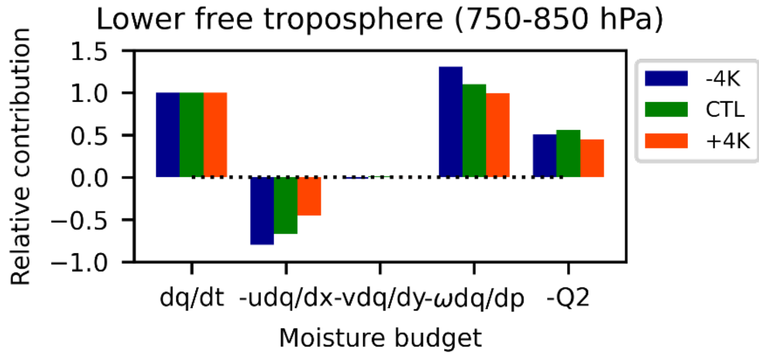

Figure S12. Contribution to KW moisture tendency from each moisture budget term averaged over the lower free troposphere (750-850 hPa) in surface warming experiments.

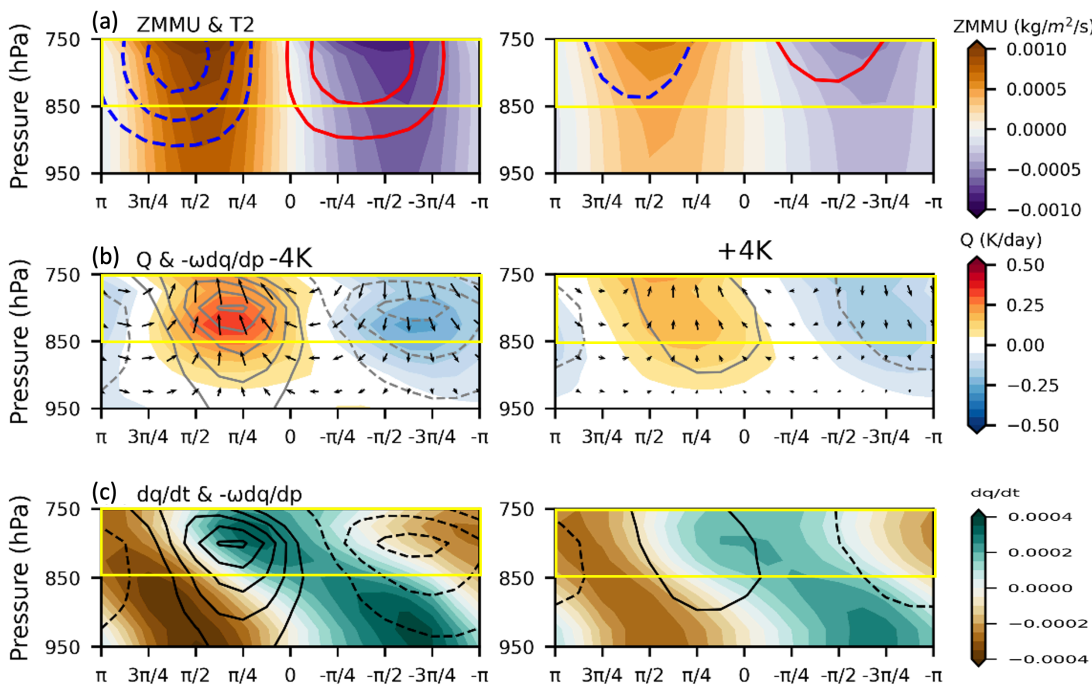

Figure S13. KW composite normalized (a) diabatic heating (shading), vertical advection of moisture (contour), zonal wind and vertical velocity (arrows), (b) updraft mass flux from the ZM deep convection scheme (shading) and second mode temperature (red and blue contour), and (c) tendency of specific humidity (shading) and vertical advection of moisture (contour). Orange boxes indicate lower troposphere (750 to 850 hPa).

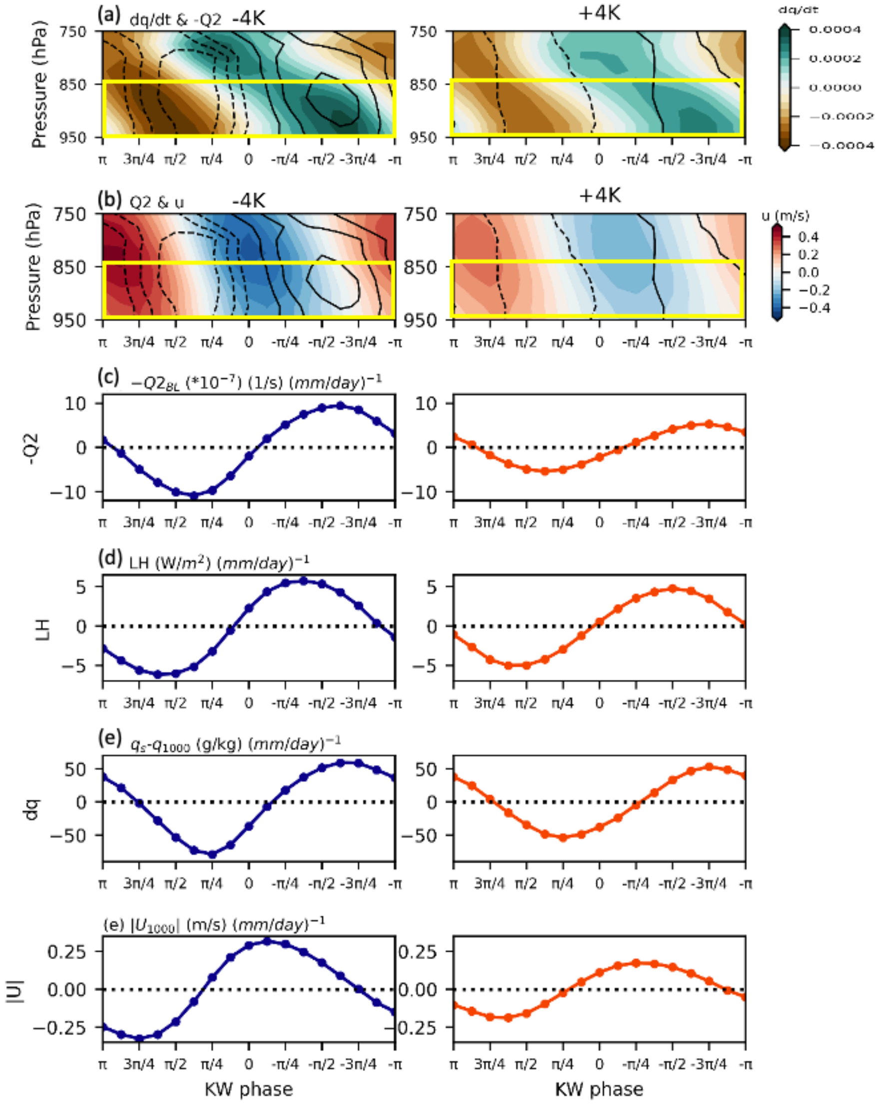

Figure S14. KW composite (a) tendency of specific humidity (shading) and apparent moisture source (contour), (a) zonal wind (shading) and apparent moisture source (contour), (b) apparent moisture source averaged over the boundary layer, (c) surface latent heat flux, (d) difference between specific humidity at 1000 hPa and saturated specific humidity at the surface, and (e) zonal wind speed at 1000 hPa. Yellow boxes indicate the boundary layer (850 to 950 hPa).

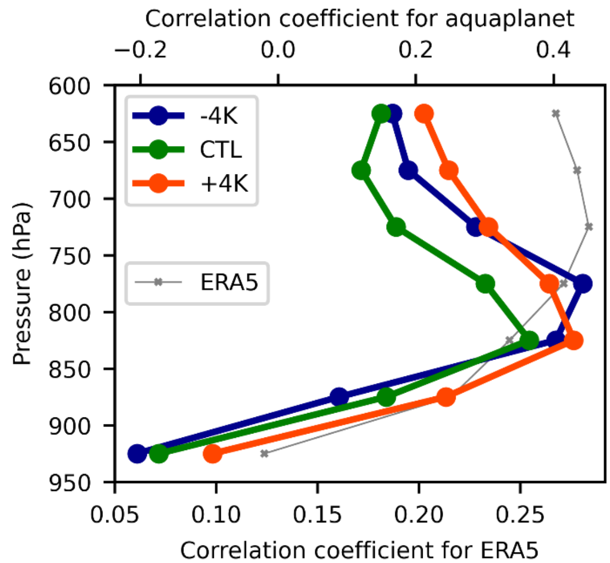

Figure S15. Correlation coefficient between the first mode diabatic heating and moisture for each pressure level in surface warming experiments and the Indian Ocean in ERA5 reanalysis.

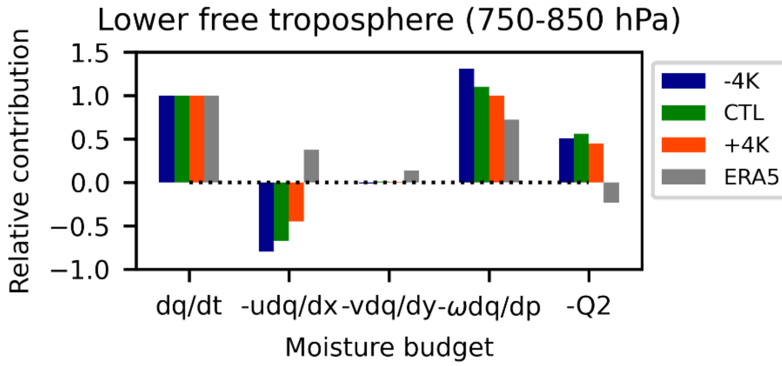

Figure S16. Contribution to KW moisture tendency from each moisture budget term averaged over the lower free troposphere (750-850 hPa) in surface warming experiments and the Indian Ocean in ERA5 reanalysis.

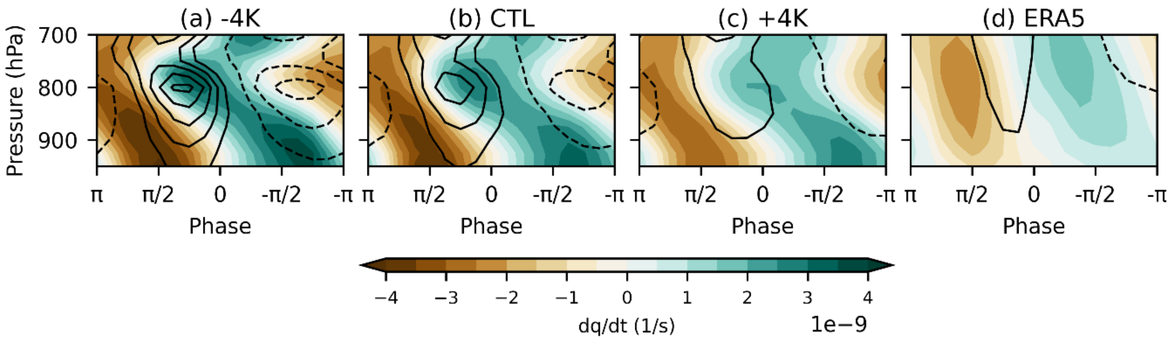

Figure S17. KW composite moisture tendency (shading) and vertical advection of moisture (shading) in (a-c) surface warming experiments and (d) in ERA5 reanalysis based on the composite in the Indian Ocean.

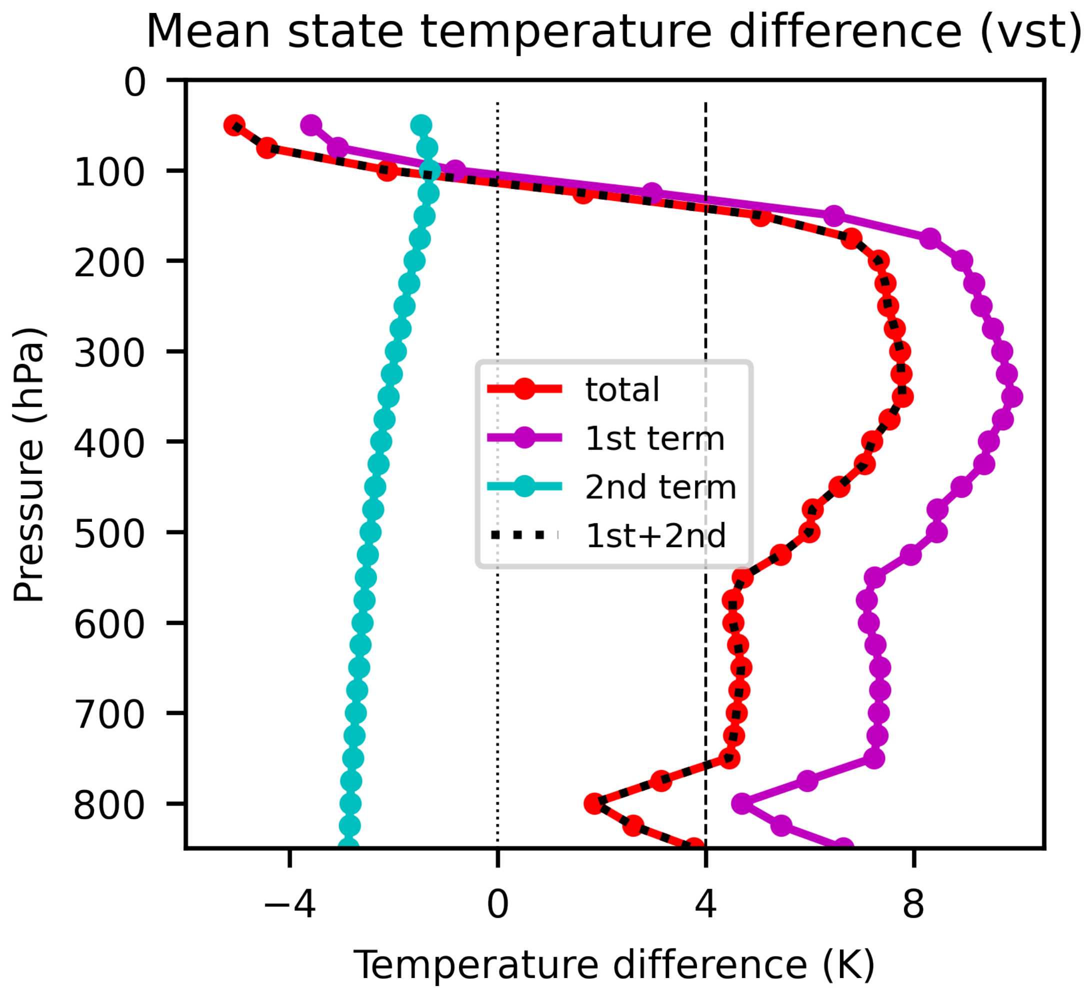

Figure S18. Decomposition of VST of temperature from the first and second terms from CTL to +4K. Note that I use beta from 500 hPa to demonstrate, but similar conclusions can be drawn from 850 hPa.

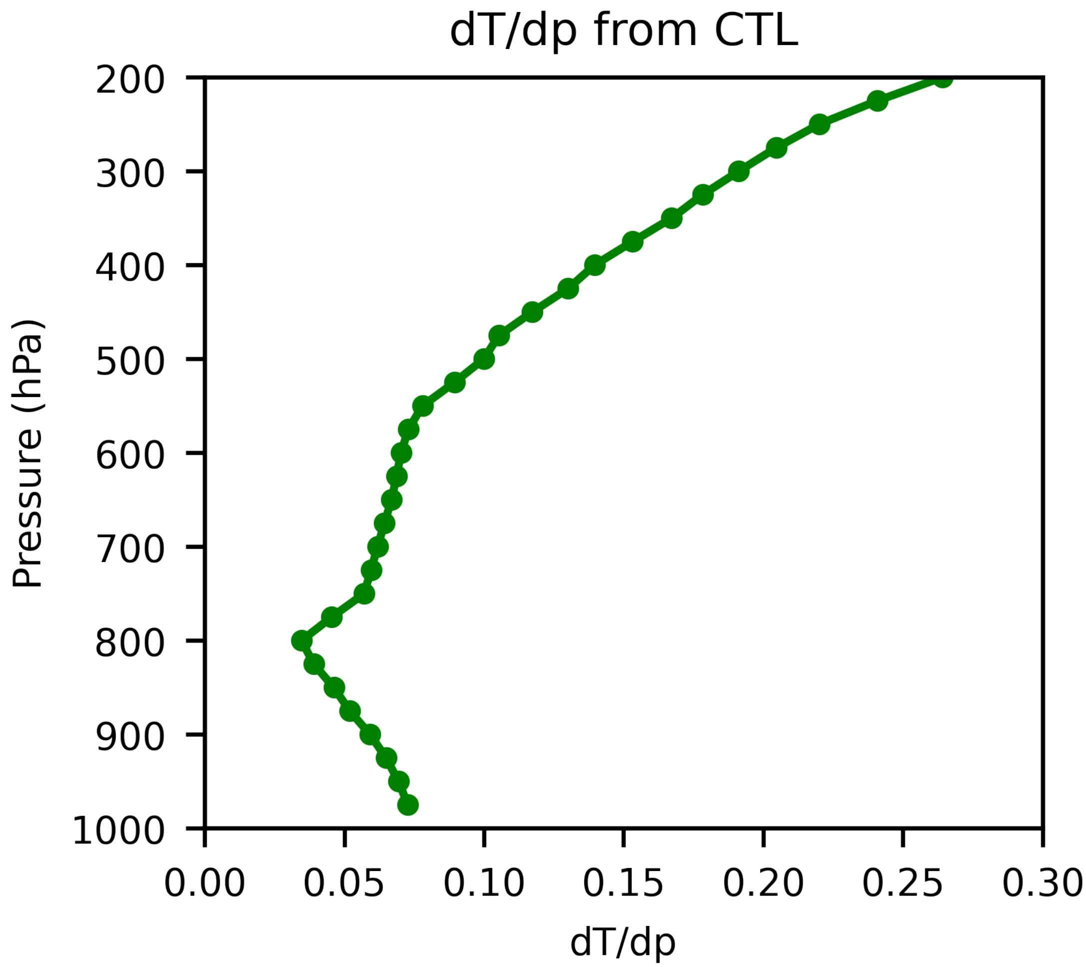

Figure S19. The vertical gradient of temperature (dT/dp, also known as static stability) in CTL simulation.